A Doppler Radar Emulator with an Application to the Detectability of Tornadic Signatures

Ryan M. May[1], Michael I. Biggerstaff[1], and Ming Xue[1,2]

[1]School of Meteorology and [2]Center for Analysis and Prediction of Storms
University of Oklahoma

Submitted to J. Atmos. Ocean. Tech.
June 2006

revised
February 2007

Corresponding author address:

Ryan May
NWC
120 David L. Boren Blvd. Suite 5900
Norman, OK 73072-7307
rmay@ou.edu

Abstract

A Doppler radar emulator was developed to simulate the expected mean returns from scanning radar, including pulse-to-pulse variability associated with changes in viewing angle and atmospheric structure. Based on the user's configuration, the emulator samples the numerical simulation output to produce simulated returned power, equivalent radar reflectivity, Doppler velocity, and Doppler spectrum width. The emulator is used to evaluate the impact of azimuthal over- and under-sampling, gate spacing, velocity and range aliasing, antenna beamwidth and sidelobes, non-standard (anomalous) pulse propagation, and wavelength-dependant Rayleigh attenuation on features of interest.

As an example, the emulator is used to evaluate the detection of the circulation associated with a tornado simulated within a supercell thunderstorm by the Advanced Regional Prediction System (ARPS). Several metrics for tornado intensity are examined, including peak Doppler velocity and axisymmetric vorticity, to determine the degradation of the tornadic signature as a function of range and azimuthal sampling intervals. For the case of a two-degree half-power beamwidth radar, like those deployed in the first integrated project of the Center for Collaborative Adaptive Sensing of the Atmosphere (CASA), the detection of the cyclonic shear associated with this simulated tornado will be difficult beyond 10-km range, if standard metrics such as azimuthal gate-to-gate shear from a single radar are used for detection.

1. Introduction

The design of a weather radar system and its scanning strategy involves tradeoffs based upon features to be observed and the cost of building and deploying the radar system. Design tradeoffs are often difficult to quantify in terms of their impacts on detecting and tracking features of interest. Moreover, the development of optimal scanning and the refinement of radar-based algorithms require large datasets to test the full range of environmental conditions and radar operating parameters to yield robust results. Recent advances in numerical modeling have made it possible to simulate convective storms at very fine scales over a broad range of environmental conditions (e.g., Wicker and Wilhelmson 1995; Lewellen et al. 1997). Coupling a software radar emulator with high-resolution numerical simulations, one can generate large sets of simulated radar data that span a wide range of radar operating characteristics. These simulated datasets can be used to quantify the impact of radar design and operational mode on the diagnosis of storm features by automated algorithms.

Many approaches have been taken previously in simulating radar data, varying in sophistication from simple time series simulation (Zrnic 1975) to reflectivity calculation (Chandrasekar and Bringi 1987; Krajewski et al. 1993) to full simulation of radar returns from each pulse (Capsoni and D'Amico 1998; Capsoni et al. 2001). Zrnic (1975) generated simulated time series radar data and Doppler spectra using an assumed Gaussian distribution of velocities within the resolution volume. Chandrasekar and Bringi (1987) looked at the variation of simulated reflectivity values as a function of raindrop size distribution parameters. Similarly, Krajewski et al. (1993) calculated values of reflectivity factor and differential reflectivity using rainfall rates from a numerical model, with an assumed drop size distribution. Neither of these studies was concerned with Doppler velocity or the impacts of scanning strategies. Wood and Brown (1997) evaluated the effects of WSR-88D (Weather Surveillance Radar-1988 Doppler,

Crum and Alberty 1993) radar scanning strategies on the sampling of mesocyclones and tornadoes. The effects of the scanning strategy were accounted for by using an effective beamwidth for the radar, which was used to scan an analytic vortex with a uniform reflectivity field. Capsoni and D'Amico (1998) simulated the pulse-to-pulse time series of radar data by combining the simulated returns from individual hydrometeors within a radar volume. This work was extended to generate polarimetric signatures by Capsoni et. al (2001). Due to the computational requirements of this approach, the radar data were generated for only a single range gate only, and thus many aspects of the scanning radar were not simulated.

This work describes a radar emulator designed to simulate the expected average returns from a scanning Doppler radar. Starting with output from a high-resolution numerical simulation, the emulator generates fields of power, equivalent reflectivity factor, Doppler velocity, and Doppler spectrum width based on the radar configuration and scanning strategy used. Here we show that the emulator is capable of simulating several radar data characteristics including: range resolution, azimuthal over- and under-sampling, non-standard (anomalous) propagation, Rayleigh attenuation, antenna sidelobes, velocity aliasing, and range aliasing.

As an example of its use for research, the emulator is applied to output from a numerical simulation of an F-3 intensity (Fujita 1971) supercell tornado simulated by the Advanced Regional Prediction System (ARPS, Xue et al. 2000; 2001) to evaluate the ability of two-degree beamwidth radars to directly detect the circulation associated with the tornado. This application is motivated by the first integrated project of the Center for Collaborative Adaptive Sensing of the Atmosphere (CASA, Brotzge et al. 2005), which has recently deployed four such radars in the Oklahoma test bed.

2. Radar emulator design

a. Emulator configuration and input

The behavior of the radar emulator is controlled by specifying radar characteristics and scanning strategy (Table 1). Note that the antenna beamwidth, gain, and wavelength are treated independently to allow for various types of antennas. The minimum detectable signal is used as a threshold to compensate for the lack of incorporation of noise (sub-grid scale turbulence and hardware electronic signals) on the quality of the emulated radar measurements. Hence, regions where signal-to-noise ratios would be expected to be low are deleted. The pulse repetition time and pulse length are given independently, but in reality, they are usually constrained by the duty cycle of the transmitter. The antenna pointing angles can be specified for either full or sector plan-position indicator (PPI) scans or range-height indicator (RHI) scans. The emulator allows for over-sampling in both azimuth (or elevation for RHI scans) and range.

The input data to the radar emulator are three-dimensional gridded fields that describe the state of the atmosphere. Wind components and mixing ratios of relevant precipitation-sized hydrometeors are required fields. Other water species can be included and used for additional scattering or attenuation. Water vapor, along with temperature and pressure, are needed for calculating the atmospheric index of refraction which is used for anomalous propagation. Temperature is also used in determining the back-scatter cross-section of hydrometeors.

b. Scattering

For computational efficiency, backscattering and extinction cross-sections per unit volume of air are pre-calculated at each model grid point. Moreover, only Rayleigh scattering by liquid hydrometeors is currently included. According to Battan (1973) and Doviak and Zrnic (1993), the Rayleigh approximation implies the following relationships for the backscattering cross section, σ_b, and the extinction cross section, σ_e, of a sphere of liquid water with diameter

D:

$$\sigma_b \approx \frac{\pi^5}{\lambda^4}|K_w|^2 D^6 \tag{1}$$

$$\sigma_e \approx \frac{\pi^2 D^3}{\lambda}\mathrm{Im}(-K_w) + \frac{2}{3}\sigma_b \tag{2}$$

$$K_w = \frac{m^2 - 1}{m^2 + 2} \tag{3}$$

where λ is radar wavelength and m is the complex index of refraction for liquid water. The emulator currently assumes a monodisperse distribution of cloud droplets and a Marshall-Palmer (1948) distribution of rain drops, which is consistent with the microphysics scheme used in many numerical models, including the ARPS. The use of a more general Gamma distribution (Ulbrich 1983) would be possible. These assumed distributions permit the calculation of the total backscattering and extinction cross sections per unit volume from the cloud water, ρ_c, and rain water, ρ_r, concentrations (in kg m^{-3}) at each grid point:

$$\frac{\sigma_b}{V} = \frac{\pi^5}{\lambda^4}|K_w|^2 (6! N_0 (\frac{\rho_r}{\pi\rho_l N_0})^{\frac{7}{4}} + \frac{48}{\pi\rho_l} R_m^3 \rho_c) \tag{4}$$

$$\frac{\sigma_e}{V} = \frac{6\pi}{\lambda\rho_l}\mathrm{Im}(-K_w)(\rho_r - \rho_c) \tag{5}$$

where ρ_l is the density of liquid water, R_m is the median radius for the cloud droplets, and N_0 is the Marshall-Palmer distribution intercept parameter. R_m and N_0 are assumed to have values of 50 μm and 8000 drops m^{-3} mm^{-1}, respectively. The Debye formula, shown by Saxton (1946) to be applicable for the microwave region, is used to calculate the complex index of refraction explicitly. The Debye formula is:

$$m^2 = \frac{\varepsilon_1 - \varepsilon_2}{1 + i(\frac{\lambda_0}{\lambda})} + \varepsilon_2 \tag{6}$$

where ε_1 is the static dielectric constant, ε_2 is the optical dielectric constant, λ_0 is the transition wavelength, and i equals $\sqrt{-1}$. Values of λ_0, ε_1, and ε_2 as a function of temperature were taken from Kerr (1951) and are based on Ryde and Ryde (1945). This formulation of m^2 allows the emulator to capture the temperature and wavelength dependencies of K_w.

It is important to note that the Rayleigh approximation has been assumed for both scattering and attenuation. The range where the Rayleigh approximation is accurate for attenuation is much more limited than that for backscatter (Battan 1973). Therefore, at wavelengths shorter than approximately 10cm, the attenuation simulated here will grossly underestimate the actual attenuation. This limitation will be addressed in future work by using scattering parameters calculated using Mie theory for spherical scatterers (Mie 1908) and/or the T-matrix method for non-spherical scatterers (Waterman 1965).

c. Sampling of input fields

To sample the virtual model atmosphere, the emulator calculates radar variables along the path of individual pulses at the interval specified by the pulse repetition time (PRT). This allows the input model fields, as well as the state of the radar (such as antenna pointing angle) to change for individual pulses. While the emulator is currently configured for a mechanically scanning antenna, pulse-by-pulse calculation can be used to emulate measurements for phased-array radar as well. The pulse generated within the emulator defines the volume of space that contributes to a sample taken along the radar beam. It is bound in elevation and azimuth by a fixed multiple of the half-power beamwidth. This multiple is chosen based on the number of sidelobes that are desired for simulation in the antenna pattern. The pulse is bound in range by the specified pulse length. This volume of space is subdivided into individual pulse elements defined in angular coordinates, such that, at the maximum range from the radar, the dimensions of each pulse element are ten percent smaller than the model grid spacing at that range. While there is

flexibility in how many subdivisions are made in the pulse element, having too many increases the computation requirements without changing the results. Sub-dividing the pulse volume into sub-elements that become larger than the grid spacing at the maximum range of the radar will result in under-sampling the model input fields and will change the emulator output.

Each pulse element is assigned values of extinction cross-section, backscattering cross section, and radial velocity that correspond to the grid point nearest to the element's location in space. Nearest neighbor sampling is chosen over interpolation to improve the computational efficiency of the emulator. Since the pulse elements are generally much smaller than the grid cells, this sampling method provides sufficient accuracy.

The radial velocity is calculated by the projection of the total wind velocity vector onto the radar beam:

$$V_r = (u \sin\theta + v \cos\theta)\cos\varphi + (w + w_t)\sin\varphi \qquad (7)$$

where V_r is the radial velocity, u is the x-component of the wind, v is the y-component of the wind, w is the z-component of the wind, w_t is the average terminal fall speed for the hydrometeors, θ is the azimuth angle measured clockwise from north, and φ is the elevation angle. The average hydrometeor terminal fall speed for the grid box is calculated as a backscatter cross-section weighted average given by:

$$w_t = \eta^{-1}\left(\frac{\rho_0}{\rho}\right)^{0.5} \int \sigma_b(D) V_t(D) N(D) dD \qquad (8)$$

where η is the total grid reflectivity, ρ is the air density of the grid box, ρ_0 is the reference density, N(D) is the drop-size distribution, and $V_t(D)$ is the terminal fallspeed as a function of diameter, which is calculated using the fitted relationship of Brandes et al. (2002):

$$V_t(D) = -0.1021 + 4.932D - 0.9551D^2 + 0.07934D^3 - 0.002362D^4 \qquad (9)$$

where V_t is in m s^{-1} and D is in mm. The weighting by backscatter cross-section makes the

terminal fall speed more representative of the velocity seen by the radar than a simple mass-weighted average.

The pulse itself is propagated through the numerical grid using a ray-tracing technique. For each range gate, the height of each pulse element is determined separately by taking into account the atmospheric index of refraction experienced by that particular ray element. This allows for differential propagation across the radar beam. The change in the height above ground, Δh, and change in range from the radar (along the surface of the Earth), Δr, can be calculated from the incremental change in range along the path, Δs, as

$$\Delta h = [h^2 + \Delta s^2 + 2h\Delta s(1 - \frac{C^2}{n^2 h^2})^{\frac{1}{2}}]^{\frac{1}{2}} \tag{10}$$

$$\Delta r = a \sin^{-1}\left[\frac{C\Delta s}{nh(h+\Delta h)}\right] \tag{11}$$

$$C = n_0 a \cos\varphi \tag{12}$$

where a is the radius of the earth, h is the previous height of the element above ground, n is the index of refraction at height h, n_0 is the index of refraction at the radar, and φ is the initial elevation angle of the element (Doviak and Zrnic 1993). The index of refraction is calculated from the model temperature, T, water vapor pressure, e, and air pressure, p, using the relation provided by Bean and Dutton (1966):

$$n = (\frac{C_d p}{T} + \frac{C_{w1} e}{T} + \frac{C_{w2} e}{T^2}) * 10^{-6} + 1 \tag{13}$$

where C_d, C_{w1}, C_{w2}, have values of 0.776 K Pa^{-1}, 0.716 K Pa^{-1}, and 3.7×10^3 K^2 Pa^{-1}, respectively. The element's range from the radar along the surface of the earth is then converted to standard two-dimensional Cartesian coordinates, which are used to determine the location of the element on the model grid.

The pulse volume is allowed to propagate through the environment as far as twice the

unambiguous range, R_a,

$$R_a = \frac{cT_s}{2} \tag{14}$$

where T_s is the PRT and c is the speed of light. Allowing the pulse to propagate $2R_a$ from the radar means that after one PRT from the time the radar is started there are two pulses propagating through the model field at any given instant. Thus, when a sample is taken, the returns from both pulses are assigned to the gate, producing the effects of range aliasing. Range aliasing can be disabled if desired.

d. The calculation of returned power

The entire pulse volume is stepped forward in range while keeping track of the total extinction cross section along the path. This running total is kept for each pulse element, which allows for the calculation of differential attenuation across the pulse. As the pulse is propagated through the model grid of the simulated atmosphere, it is periodically sampled at an interval in range dictated by the specified gate spacing. This allows for the gate and pulse lengths to be independent. When a pulse sample is taken, three values are calculated: power, power-weighted average radial velocity, and power-weighted radial velocity variance. The power-weightings are performed over all of the pulse elements as follows:

$$\overline{V}_r = \frac{\sum_i P_i V_i}{\sum_i P_i} \tag{15}$$

$$\sigma_{vr} = \frac{\sum_i P_i V_i^2}{\sum_i P_i} - \overline{V}_r^2 \tag{16}$$

where $\overline{V}_r$ is the power-weighted average radial velocity, σ_{vr} is the power-weighted variance of radial velocities, P_i is the power for a particular pulse element, and V_i is the radial velocity for a

particular pulse element. The estimate of variance here, σ_{vr}, is not unbiased, but is chosen to simplify the computations. Since values from thousands of pulse elements are used in the calculation, the difference between biased and unbiased estimates is negligible.

As given in Doviak and Zrnic (1993), the power, P, for a sample taken at range r_0 is given by

$$P(r_0) = \iiint \eta(r) I(r_0, r) dV \tag{17}$$

where

$$I(r_0, r) = \frac{P_t g^2 \lambda^2 f^4(\theta, \varphi) |W(r_0, r)|^2}{(4\pi)^3 l^2(r) r^4} \tag{18}$$

$$dV = r^2 dr \sin\varphi d\varphi d\theta \tag{19}$$

and P_t is the transmitted power, g is the system gain, λ is the wavelength, r is range from the radar, l is the attenuation factor, f^2 is the normalized antenna pattern, η is the reflectivity (backscattering cross section per unit volume), θ is the azimuth angle relative to the beam center, φ is the elevation angle relative to beam center, and W is the range weighting function. The emulator approximates this integral with a sum over the finite elements within the pulse volume,

$$P(r_0) = \frac{P_t g^2 \lambda^2}{(4\pi)^3} \sum_i \frac{f_i^4 W_i^2 \eta_i \Delta V_i}{l_i^2 r_i^2} \tag{20}$$

where ΔV is the volume of a pulse element, and all quantities subscripted with i are values for a particular pulse element. The emulator assumes a Gaussian range weighting function and a normalized antenna pattern with the following form (Doviak and Zrnic 1993)

$$f^2(\theta) = \left[\frac{8 J_2(\pi D_a \sin\theta / \lambda)}{(\pi D_a \sin\theta / \lambda)^2} \right]^2 \tag{21}$$

where J_2 is the second-order Bessel function of the first kind, θ is the angular offset from

boresight and D_a is the diameter of the antenna. D_a for (21) above can be calculated from the half-power beamwidth, θ_1, as

$$D_a = \frac{1.27\lambda}{\theta_1} \tag{22}$$

where λ is the wavelength. Doviak and Zrnic (1993) state that (21) describes the antenna pattern for the first few sidelobes quite well for a parabolic antenna. However, (21) is limited in that it gives sidelobes of a fixed level and location (e.g. Figure 1), prohibiting configuration of sidelobes with arbitrary magnitude.

e. Moment calculation

The sampling of model data is repeated for the number of pulses that are to be averaged for a radial of data, as specified by the scanning strategy. Moment data (power, Doppler velocity, and Doppler spectrum width) are then generated for at each range gate along the radial. Power is calculated as the average of all power samples for the specified number of pulses at that range gate. Note that this is the expected mean power that an actual weather radar would produce if random power fluctuations were successfully removed by the pulse averaging and the radar system had no noise.

Radial velocity is calculated as the power-weighted average of all velocity samples (one per pulse) at that range gate. To emulate velocity aliasing, this average is restricted to a value within the Nyquist interval and is given by

$$V_a = V_r + 2nV_{NYQ} \tag{23a}$$

where

$$n = 0 \text{ for } |V_r| \le V_{NYQ} \tag{23b}$$

$$n = \frac{V_{NYQ} - V_r}{2V_{NYQ}} - 1 \text{ for } V_r > V_{NYQ} \tag{23c}$$

$$n = \frac{-V_{NYQ} - V_r}{2V_{NYQ}} + 1 \text{ for } V_r < -V_{NYQ} \tag{23d}$$

where V_a is the aliased velocity value, V_r is the original (unaliased) radial velocity, V_{NYQ} is the Nyquist (or aliasing) velocity, and n, an integer, is the number of Nyquist intervals by which the V_a differs from V_r. One advantage of emulated data is that the unaliased Doppler velocity is known. Spectrum width is calculated as the power-weighted average of the variance for each sample, which is the variance of all velocity values within the pulse. Initial attempts at emulating spectrum width used only the variance of the individual velocity samples that were themselves an average over the entire pulse. That approach produced unreasonably low spectrum width. By taking into account the variance of all velocity values within all pulses, the spectrum width takes into account the effect of antenna rotation and wind shear across the radar beam. However, we have neglected sub-grid scale atmospheric turbulence. Moreover, since the emulator does not generate a true power spectrum at each range gate, the emulated spectrum width does not take into account a limited Nyquist interval or the pulse-to-pulse variability associated with random phase changes from scatterers moving relative to the transmitted wavelength. In addition to the three moments above, equivalent reflectivity factor (Z_e) is calculated from the average power, P_r, using

$$Z_e = \frac{2^{10}(\ln 2)\lambda^2 r^2 \overline{P_r}}{\pi^3 P_t g^2 \theta_1^2 c\tau |K_w|^2} \tag{24}$$

where τ is the pulse duration.

3. Demonstration of emulator capabilities

Emulated data were generated for different radar characteristics to illustrate the emulator's capabilities and to demonstrate the impact of radar design on data quality. The input is from a numerical simulation of a supercell thunderstorm produced using the Advanced

Regional Prediction System (ARPS, Xue et al. 2000; 2001). The ARPS is a fully compressible and nonhydrostatic prediction model and its prognostic state variables include wind components u, v, w, potential temperature θ, pressure p, the mixing ratios for water vapor q_v, cloud water q_c, rainwater q_r, cloud ice q_i, snow q_s and hail q_h, plus the turbulent kinetic energy used by the 1.5-order subgrid-scale turbulent closure scheme.

For the current simulation, only liquid-phase, Kessler (1969) microphysics is used. The simulation had a horizontal grid spacing of 50 m over a 48 km by 48 km domain and a vertically stretched grid that goes from the surface to 16 km. The stretching is specified by a hyperbolic tangent function, having a minimum spacing of 20 m at the surface, 380 m spacing at the top of the model, and a mean spacing of 200 m (Xue et al. 1995). The model thunderstorm was initiated by a thermal bubble in a horizontally homogeneous environment defined by the 20 May 1977 Del City, Oklahoma supercell sounding reported in Ray et al. (1981). Detailed analysis of the simulated storm is unimportant here as the simulation serves only as input to the emulator. Furthermore, only a single time step taken during the most intense portion of the tornadic stage of the simulated storm is used. The impact of storm evolution on radar-derived storm structure will be the subject of future studies.

Figure 2 shows the rain water mixing ratio and storm-relative velocity at the surface at 13500 seconds into the simulation, the time used to produce the emulated data. An intense supercell thunderstorm with characteristic v-notch and hook (Lemon and Doswell 1979) in the rain water field is evident. The simulated tornado vortex is about 200 m in diameter, with maximum winds of about 75 m s^{-1}.

Table 2 lists the parameters used to define the radar and scanning strategy in each of the experiments discussed below.

a. Control experiment for S-band radar with 1° beamwidth

The control experiment (CNTL), against which other radar configurations are compared, assumes characteristics similar to those of the United States National Weather Service WSR-88D (Crum and Alberty 1993) operational weather radars. The WSR-88Ds operate at a nominal wavelength of 10 cm with a peak power of 750 kW and have a nominal half-power beamwidth of one degree. The current operational scanning strategy uses a one-degree azimuthal sampling interval (which is close to the beamwidth), with range gates spaced 250 m apart. For these experiments, the radar is located 20 km north of the southern edge of the model domain and 31 km east of the western edge of the domain, or about 10km northeast of the center of the tornadic circulation. Except where noted, the antenna has no sidelobes but is restricted to the area between the first nulls in the antenna pattern, keeping the full mainlobe of the antenna. The width of this region for a one degree half-power beamwidth antenna is approximately three degrees. Plan Position Indicators (PPIs) of emulated power, equivalent reflectivity factor (Z_e), Doppler radial velocity, and spectrum width (Figure 3) for this experiment show the familiar reflectivity structure (Figure 3b) of a supercell thunderstorm, with a pronounced hook echo (magnified in Figure 4). A pronounced mesocyclone circulation (Figure 3c, Figure 4c), with a small region of high gate-to-gate shear corresponding to the tornado, was found at the tip of the hook echo. The spectrum width (Figure 3d, Figure 4d) was relatively low, 1-3 m s^{-1}, for most of the storm. However, the spectrum width was higher (> 4 m s^{-1}) in the region of the mesocyclone, reaching a maximum of ~20 m s^{-1} around the tornado. It should also be noted that the Doppler velocity field for this experiment exhibits almost no aliasing, except for a single velocity gate, due to the high Nyquist velocity (37.5 m s^{-1}) of the CNTL run. Even at this range, the 75 m s^{-1} flow in the simulated tornado was significantly reduced by averaging across the one-degree half-power beamwidth. Similar reduction in vortex strength by beam averaging was noted by Wood

and Brown (1997).

b. Oversampling in azimuth

Experiment EXP2 (Table 2) is identical to CNTL, except fewer pulses (50 instead of 75) are used to generate a radial, and the antenna is rotated at 15 instead of 20 degrees per second, yielding data that are azimuthally oversampled relative to the beamwidth. This difference in azimuthal sampling resulted in differences in the observed structure of the storm, especially in the tornadic region (Figure 5). Overall, azimuthal over-sampling yielded finer-scale structure of the storm (c.f. Figure 4). Of particular interest are the velocity measurements around the tornado; the oversampled data produce higher inbound and outbound velocities than the beam-matched CNTL case. These increases in velocity values, though minimal, are due to the decreased region that is averaged, which allows the peak velocity values in the tornado to contribute more to the sampled Doppler velocity value. Wood et al. (2001) and Brown et al. (2002) report a similar result for an idealized Rankine vortex flow and a simpler radar emulator. Using time-series data taken from a WSR-88D during a tornadic supercell, Wood et al. (2001) demonstrated that over-sampling by a factor of two increased observed mesocyclone strength by 10-50% relative to standard azimuthal sampling for one-third of the mesocyclones detected.

c. Effects of gate length

Experiment EXP3 (Figure 6) differs from CNTL by using a smaller gate length, 125 m instead of 250 m, and a correspondingly smaller pulse length, 0.75 μs instead of 1.5 μs, resulting in a higher range resolution. As in experiment EXP2, the shorter sampling interval in the radial direction results in the elucidation of finer scale flow, especially in the region of the tornado. Due to the smaller region sampled (and averaged) in range, higher inbound and outbound velocity values are obtained, though not as high as the azimuthally oversampling case. The latter is expected because azimuthal oversampling is more effective in capturing the extreme values of

inbound and outbound velocities in quasi-axisymmetric flow. This fact was also the motivation of the work of Xue et al. (2006b).

d. Effects of sidelobes

Experiment 4 repeated the CNTL experiment with the pulse expanded to six degrees in azimuth, which included the first two antenna sidelobes. For the antenna pattern used here, the first sidelobe had a one-way gain that was 28 dB less than the peak of the main lobe. Since ground clutter was not included, this experiment exhibited only minor differences from CNTL (Figure 7 and Figure 8). Regions with the strongest reflectivity gradients exhibited a few tenths of a decibel change in returned power and a few tenths of a meter per second difference in wind speed. The area around the tornado had almost no change in diagnosed velocity, suggesting that the WSR-88D velocity measurements in such storms are not strongly affected by sidelobes in the absence of ground clutter.

While the increase in volume contributing to returned power in EXP4 should have led to consistently higher values, there are a few places where less power was found. The lower power results from slight changes in the antenna gain weighting assigned to individual grid elements illuminated by the radar beam between the two runs. In essence, the center of the beam is not located in exactly the same place due to truncation in the numerical calculations of the beam projection through the model grid. These small errors led to places in which the sidelobes run had lower power than the CNTL run without sidelobes. We speculate that once ground clutter is included the enhanced return from the ground will overwhelm this numerical artifact and result in higher reflectivity uniformly across the radar domain at small elevation angles.

e. Experiment with PRF and effects on velocity aliasing

In experiment EXP5, the pulse repetition frequency (PRF) was set to 1000 Hz instead of the 1500 Hz in CNTL, and 50 pulses were used for each radial instead of 75, to keep the

azimuthal sampling interval the same (one degree). This changes the Nyquist velocity from 37.5 m s^{-1} for CNTL to 25 m s^{-1} for EXP5. Figure 9c shows a PPI of the Doppler velocity for this case. The reduced Nyquist velocity causes more velocity aliasing, especially in the mesocyclone and tornado region. There are also subtle differences in the Z_e (Figure 9b) and spectrum width (Figure 9d) fields, which are caused by the change to a lower PRF and using fewer samples to generate a radial of data. This experiment illustrates the advantage of using high PRFs to reduce velocity aliasing. This becomes particularly important at shorter wavelengths, since the Nyquist velocity scales linearly with the transmitted wavelength.

f. Experiment with beamwidth

In EXP6 the half-power beamwidth was increased from one to two degrees (effectively halving the diameter of the dish) while keeping the azimuthal sampling interval the same. This effectively yields azimuthally oversampled data, since the one-degree azimuthal sampling interval is smaller than the antenna's half-power beamwidth (Figure 10). Comparing the data with those CNTL (Figure 4), it is clear that the broader beam decreases the peak velocities retrieved by the emulator within the tornado (Figure 10c). Specifically, the maximum outbound velocity is decreased from 38 to 31 m s^{-1}. Changing the half-power beamwidth also increases the spectrum width in the entire region of mesocyclone, which is a consequence of the larger sampling volumes.

g. Second trip echoes and range aliasing

The purpose of EXP7 was to demonstrate the emulator's ability to simulate range aliasing. In this case, the radar is located approximately 100 km from the storm's mesocyclone. Otherwise the scanning strategy is the same as CNTL, which had an unambiguous range of 100 km. With this scanning strategy, part of the storm is located beyond the unambiguous range, resulting in second trip echoes from 0 to 35 km range (Figure 11). These echoes look very

narrow as a result of the fixed angular resolution of the data, which causes distortion since the data are assigned to a much closer range than their actual location. It is important to note that currently the velocities from the second trip echoes are determined by assuming a fixed-phase transmitter, like a klystron, which makes the Doppler velocities and spectrum widths of the second trip echoes coherent. Emulation of a random phase transmitter, like a magnetron, could be accomplished by assigning a random value of velocity for each sample of the radar pulse for the second trip echo.

h. Radar wavelength and effects on attenuation and velocity aliasing

EXP8 was identical to CNTL, except that the transmitted wavelength of the radar was changed from 10 cm (S-band) to 3 cm (X-band). Comparing the returned power in EXP8 (Figure 12a) to that in CNTL (Figure 3a) reveals the effects of Rayleigh attenuation at X-band. On the radar side of the storm, the X-band returned power is approximately 10 dB greater than S-band (Figure 13), as expected from the dependence of returned power on the transmitted wavelength (Eq. 16). On the opposite side of the storm from the radar, this difference decreases to ~3 dB, corresponding to ~7 dB decrease in the returned power at X-band due to Rayleigh attenuation. As previously mentioned, the Rayleigh approximation underestimates attenuation at shorter wavelengths, so the actual attenuation at X-band for such a storm would be much greater. Here we are merely demonstrating the ability of the emulator to properly handle the propagation effects. The current algorithm could easily incorporate extinction cross-sections from Mie (1908) or T-matrix (Waterman 1965) calculations. In addition to non-Rayleigh attenuation, the model does not include ice microphysics. Hence, wet hail, a strong attenuator (Battan 1971), is not included.

Another significant difference between S-band and X-band is the amount of velocity aliasing (Figure 12c). At X-band, the Nyquist velocity for a given PRF is 30 percent of that at S-

band; in EXP8, the Nyquist velocity is 11.25 m s^{-1}. Consequently, the EXP8 Doppler velocity field shows a large amount of aliasing, with some regions, such as the storm's mesocyclone, exhibiting aliasing by more than one Nyquist interval.

4. Application to tornado detection

To illustrate the research and operational value of the radar emulator, the detectability of tornadic signatures is examined as a function of the radar range from the tornado and the azimuthal sampling interval. The emulated radar characteristics (Table 3) follow those of the Integrated Project 1 (IP1) radars deployed by the Collaborative Adaptive Sensing of the Atmosphere (CASA) Engineering Research Center (Brotzge et al. 2005). To keep cost low, these radars have a broad beam (2° half-power beamwidth), use relatively low power (25 kW), and operate at X-band. One of the goals of CASA is to improve the detection of low-level hazardous weather, such as tornadoes, by placing the radars close to each other and by performing collaborative adaptive sampling of the lowest 3 km of the atmosphere. The average radar spacing of the IP1 network is about 30 km.

Using the known location and intensity of the tornado in the model as a baseline, this study examines the values of several tornado intensity metrics, including maximum velocity (V_{max}), maximum radial velocity difference (ΔV), diameter (D), and axisymmetric vorticity (ζ_a), as determined directly from the emulated radial velocity data. They are examined as functions of range (3, 10, 30, and 50 km) from the tornado, using both azimuthally matched sampling (two degree intervals) and oversampling (at one degree intervals). The axisymmetric vorticity is defined as the vorticity for an axisymmetric vortex having the same ΔV and diameter as the tornado, and is given by

$$\zeta_a = \frac{2\Delta V}{D}. \tag{25}$$

The intensity parameters are used to quantify the range dependency of tornado detection by two-degree-beam X-band radars. To eliminate the impact of dealiasing algorithms, this quantitative analysis assumes perfectly dealiased Doppler velocities, and hence represents the best-case scenario. Furthermore, the known location of the tornado is used to choose the gates for the calculation of the parameters, as opposed to choosing a location based on the position of the velocity maxima in the data. The values of these parameters for all cases, with different range and azimuthal sampling combinations, are listed in

Table 4. It should also be noted that the viewing angle chosen here (from northeast) minimizes the impact of attenuation at X-band.

At 3-km range, the tornado can be clearly identified in both the matched and over-sampled moment data (Figure 14 and 15). The tornado resides in the tip of a well defined hook echo in a region of enhanced spectrum width. At this range, the strong flow within the tornado can be diagnosed even in the aliased Doppler radial velocity field, especially when the storm is azimuthally oversampled by the radar beam. Indeed, the over-sampled unaliased velocity field (Figure 15d) shows separated inbound and outbound velocity maxima in the tornado vortex. Separation between maximum radial velocities is a useful criterion for resolving a tornadic circulation. Even at this close range, however, the peak Doppler velocity of the tornado measured by the radar (

Table 4) is greatly decreased from the true value of 78 m s^{-1}. The distance between peak Doppler velocities, 216 m, agrees well with the ~200m distance between velocity maxima in the model field. Axisymmetric vorticities of 0.864 s^{-1} and 1.024 s^{-1} for the matched and oversampled cases, respectively, further indicate that the tornadic circulation is well resolved by the two-degree half-power beamwidth radar at 3-km range.

Moving the radar to 10 km away from the tornado resulted in degradation of the radar derived structure as the geometric width of the beam increased (Figure 16 and Figure 17). While the hook echo and maxima in spectrum width were still fairly well resolved in the matched sampling case, the peak Doppler velocities associated with the tornado were located much further apart (705 m), with the peak velocity down to 35.2 m s^{-1}. Consequently, the estimated vorticity decreased to 0.163 s^{-1}, or 20 percent of the value obtained at 3-km range. It should be noted that the peak inbound velocity measured with the tornado was only 22.4 m s^{-1}, less than the 24.1 m s^{-1} inbound velocity associated with the mesocyclone. It is only when the storm was azimuthally oversampled that the tornadic circulation was resolved at 10-km range with the current radar system. With one-degree azimuthal sampling (Figure 17), the distance between the velocity maxima decreased to 529 m, which was the main factor for the increase in the axisymmetric vorticity to 0.237 s^{-1}.

At 30-km range with matched sampling, the structure of the hook echo and spectrum width field is so degraded that the location of the tornado is no longer well-diagnosed by the radar parameters (Figure 18). Even the non-aliased velocity field no longer shows separate velocity maxima for the tornado and mesocyclone. Instead, a single maximum is located several gates away from the known location of the tornado. The tornado-scale flow is no longer resolved because the half-power beamwidth is over 1 km wide at this range, roughly five times the diameter of the tornado. Also at this range, the poor resolution of the data makes

distinguishing storm shear from regions of aliased velocity a challenge (Figure 18c). Using the known location of the tornado, a vorticity estimate of 0.064 s^{-1} is calculated for this circulation. Such a low vorticity estimate would likely not be associated with a strong tornadic mesocyclone. It should be noted that the inbound velocity measured and used in the calculation is only 1.6 m s^{-1}. Even when oversampling is performed (Figure 19) the tornadic circulation is still not resolved by a two-degree beamwidth radar when it is located 30km away. While the separation between the maximum inbound and outbound velocities in the mesocyclone and a region of enhanced spectrum width exists, there is no indication of a tornado vortex signature (Brown et al. 1978). Furthermore, dealiasing the X-band radial velocity field becomes challenging as the beam containing the tornado appears to be embedded in a broad-scale region of aliased inbound velocities. In reality, the minimum in radial velocity associated with the tornado separates aliased inbound velocities from the true receding flow.

At 50-km range, the half-power beamwidth is 1.7 km across, reducing even the mesocyclone-scale circulation to gate-to-gate shear and completely obscuring the tornado-scale flow (Figure 20). It would be very difficult to detect reliably a tornado with the size and intensity as in the simulation using only the moment data at this range.

5. Conclusions

A Doppler radar emulator based on Rayleigh scattering has been developed that simulates a wide range of radar operating characteristics, including range and azimuthal oversampling, velocity and range aliasing, Rayleigh attenuation, second trip echoes, antenna sidelobes, and anomalous propagation. The emulator calculates returned power, equivalent radar reflectivity factor, Doppler velocity, and Doppler spectrum width from cloud model output containing fields of wind, temperature, moisture, and hydrometeor species. The capabilities of the emulator are demonstrated using a high spatial resolution simulation of a tornado embedded within a supercell

thunderstorm. It is shown that the emulator is a useful tool for evaluating the capabilities and tradeoffs in the design, deployment, and operation of radar systems. Given that the emulator can produce numerous synthetic data sets for a wide range of storm types and radar characteristics, we believe that such a tool can be a significant aid in the development of radar algorithms. Such realistically emulated data can also be used in observing system simulation experiments (OSSEs) such as those of Xue et al (2006a) for examining the potential impact of radar data on thunderstorm analysis and prediction.

Using the output from a 50-m horizontal-resolution simulation of a supercell storm that explicitly resolves an F-3 intensity tornado of about 200 m in diameter, the basic capabilities of the emulator are first tested in a set of experiments that examines the effects of radar wavelength, beamwidth, azimuthal oversampling, gate length, sidelobes, pulse repetition frequency, and the effects of velocity and range aliasing. Results consistent with theory are observed from the simulated data.

As an example of the emulator's many potential applications, the detection of the simulated tornado described above by a two-degree half-power beamwidth X-band radar is examined. The emulated data shows that the strength of the diagnosed tornado circulation decreases rapidly with range, with the tornado-scale flow becoming unresolved at and beyond 30 km. Azimuthal oversampling improves the ability to diagnose the tornado vortex, especially from the 10-km to 30-km ranges. At shorter ranges, the two-degree beam-matched azimuthal sampling is sufficient. It is important to note that the simulated tornado examined here represents the top 10% of tornadoes occurring in nature in terms of intensity. The much more prevalent weaker and/or smaller tornadoes will be even harder to detect.

A significant problem demonstrated by the emulator is the impact of velocity aliasing at X-band on the potential diagnosis of the circulations. Correct dealiasing is crucial to tornado

detection when the detection algorithm mainly relies on the radial velocity data (e.g., Burgess et al. 1993; Liu et al. 2006). Any method that can increase the effective Nyquist velocity, such as the use of staggered-PRT (Gray et al. 1989), would likely be helpful.

Future studies will include more radar operating parameters as well as the use of objective algorithms to evaluate tornado detection for broad-beam X-band radars. This work is motivated by the Integrated Project I (IP1) of the Collaborative Adaptive Sensing of the Atmosphere (CASA; Brotzge et al. 2005) Engineering Research Center that has recently deployed four two-degree half-power beamwidth X-band radars in central Oklahoma. One of the goals of such inexpensive networks is tornado detection, based on the promise of being able to observe at low altitudes (0 to 3 km) and at short ranges (less than 30 km), and do so in a collaborative and adaptive manner. In the future, the radar emulator will be further enhanced to include Mie scattering, as well as scattering from ice-phase hydrometeors, and the antenna routine will be modified to allow for emulation (using many model time steps) of electronically steered phased-array radars that can point the beam in arbitrary directions on a pulse-to-pulse basis. This will enable applied research in the Phased Array Radar (Forsyth et al. 2005) program and further enhance the educational utility of the radar emulator.

Acknowledgements This work was supported by graduate research fellowships sponsored by the Office of Naval Research through the AMS and by the Army Research Office through the National Defense Science and Engineering Graduate Fellowship program. Partial support was also provided by NSF grant EEC-0313747 to the ERC of Collaborative Adaptive Sensing of the Atmosphere (CASA). M. Biggerstaff was supported by NSF grants ATM-0619715, ATM-0410564 and ATM-0618727 while M. Xue was supported by NSF grants ATM-0129892, ATM-0331594, ATM-0331756, and ATM-0530814. The authors would also like to thank two anonymous reviewers whose many comments helped improve the quality of this work.

References

Bean, B. R., and E. J. Dutton, 1966: Radio Meteorology. Monograph No. 92, National Bureau of Standards, 431pp.

Battan, L. J., 1971: Radar attenuation by wet ice spheres. J. App. Meteor., 10, 247-252.

Battan, L. J., 1973: Radar Observation of the Atmosphere. Univ. of Chicago Press, Chicago, 324pp.

Brandes, E. A., G. Zhang, and J. Vivekanandan, 2002: Experiments in rainfall estimation with a polarimetric radar in a subtropical environment. J. Appl. Meteor., 41, 674–685.

Brotzge, J. A., K. Brewster, B. Johnson, B. Philips, M. Preston, D. Westbrook, and M. Zink, 2005: CASA's first testbed: Integrated project #1 (IP1). Preprints, 32nd Conf. on Radar Meteor. Albuquerque, New Mexico. Amer. Meteor. Soc., CD-ROM, 14R.2.

Brown R. A., D. W. Burgess, and L. R. Lemon, 1978: Tornado detection by pulsed Doppler radar. Mon. Wea. Rev., 106, 29–38.

-----, V. T. Wood, and D. Sirmans, 2002: Improved tornado detection using simulated and actual WSR-88D data with enhanced resolution. J. Atmos. Ocean. Tech., 19, 1759-1771.

Burgess, D. W., R. J. Donaldson, Jr., and P. R. Desrochers, 1993: Tornado detection and warning by radar. In The Tornado: Its Structure, Dynamics, Prediction and Hazards, C. Church, D. Burges, C. Doswell, and R. Davies-Jones, Eds., Amer. Geophys. Union, 203-221.

Capsoni, C., and M. D'Amico, 1998: A physically based radar simulator. J. Atmos. Oceanic Technol., 15, 593-598.

-----, -----, and R. Nebuloni, 2001: A multi-parameter polarimetric radar simulator. J. Atmos. Oceanic Technol., 18, 1799-1809.

Chandrasekar, V., and V. N. Bringi, 1987: Simulation of radar reflectivity and surface measurements of rainfall. J. Atmos. Oceanic Technol., 4, 464-478.

Crum, T. D., and R. L. Alberty, 1993: The WSR-88D and the WSR-88D operational support facility. Bull. Amer. Meteor. Soc., 74, 1669-1687.

Doviak, R. J., and D. S. Zrnic, 1993: Doppler Radar and Weather Observations. Academic Press, San Diego, 562pp.

Forsyth, D.E., J.F. Kimpel, D.S. Zrnic, R. Ferek, J. F. Heimer, T. McNellis, J. E. Crain, A. M. Shapiro, R. J. Vogt and W. Benner, 2005: The National Weather Radar Testbed (Phased-Array). Preprints, 32nd Conf. Radar Meteor., Albuquerque, NM, Amer. Meteor. Soc., CD-ROM, 12R.3.

Gray, G., B. Lewis, J. Vinson, and F. Pratte, 1989: A real-time implementation of staggered PRT velocity unfolding. J. Atmos. Oceanic Technol. 6, 186-187.

Kerr, D. E., 1951: Propagation of short radio waves, Vol. 13. MIT Rad. Lab. Ser., New York, McGraw-Hill, 728 pp.

Kessler, E., 1969: On the Distribution and Continuity of Water Substance in Atmospheric Circulations. Meteor. Monogr., No. 32, Amer. Meteor. Soc., 84 pp.

Krajewski, W. F., R. Raghavan, and V. Chandrasekar, 1993: Physically based simulation of radar rainfall data using a space-time rainfall model. J. Appl. Meteor., 32, 268-283.

Lemon, L. R., and C. A. Doswell III, 1979: Severe thunderstorm evolution and mesocyclone structure as related to tornadogenesis. Mon. Wea. Rev., 107, 1184-1197.

Lewellen, W. S., D. C. Lewellen, and R. I. Sykes, 1997: Large-eddy simulation of a tornado's interaction with the surface. J. Atmos. Sci., 54, 581-605.

Liu, S., M. Xue, and Q. Xu, 2006: Using wavelet analysis to detect tornadoes from Doppler radar radial-velocity observations. J. Atmos. Ocean Tech., under review.

Marshall, J. S., and W. M. Palmer, 1948: The distribution of raindrops with size. J. Meteor., 5, 165-166.

Mie, G., 1908: Beigrade zur Optik truber Medien, speziell kolloidaler Metallosungen. Ann. Phys., 25, 377–445.

Ray, P. S., B. Johnson, K. W. Johnson, J. S. Bradberry, J. J. Stephens, K. K. Wagner, R. B. Wilhelmson, and J. B. Klemp, 1981: The morphology of severe tornadic storms on 20 May 1977. J. Atmos. Sci., 38, 1643-1663.

Ryde, J. W., and D. Ryde, 1945: Attenuation of centimeter and millimeter waves by rain, hail, fogs, and clouds. General Elec. Co. Rep. No. 8670.

Saxton, J. A., 1946: Meteorological factors in radio-wave propagation. London, The Physical Society, 278-325.

Ulbrich, C. W., 1983: Natural variations in the analytical form of the raindrop size distribution. J. Appl. Meteor., 22, 1764-1775.

Waterman, P. C., 1965: Matrix formulation of electromagnetic scattering. Proc. IEEE, 53, 805–812.

Wicker, L. J. and R. B. Wilhelmson, 1995: Simulation and analysis of tornado development and decay within a three-dimensional supercell thunderstorm. J. Atmos. Sci., 52, 2675-2703.

Wood, V. T., and R. A. Brown, 1997: Effects of radar sampling on single-Doppler velocity signatures of mesocyclones and tornadoes. Wea. Forecasting, 12, 928-938.

-----, -----, and D. Sirmans, 2001: Technique for improving detection of WSR-88D mesocyclone signatures by increasing angular sampling. Wea. Forecasting, 16, 177-184.

Xue, M., K. K. Droegemeier, V. Wong, A. Shapiro, and K. Brewster, 1995: ARPS Version 4.0 User's Guide. [Available at http://www.caps.ou.edu/ARPS], 380 pp.

-----, -----, -----: The Advanced Regional Prediction System (ARPS) - A multiscale nonhydrostatic atmospheric simulation and prediction tool. Part I: Model dynamics and verification. Meteor. Atmos. Physics., 75, 161-193.

-----, -----, -----, A. Shapiro, K. Brewster, F. Carr, D. Weber, Y. Liu, and D. Wang, 2001: The Advanced Regional Prediction System (ARPS) - A multi-scale nonhydrostatic atmospheric simulation and prediction tool. Part II: Model physics and applications. Meteor. Atmos. Phys., 76, 143-166.

-----, M. Tong, and K. K. Droegemeier, 2006a: An OSSE framework based on the ensemble square-root Kalman filter for evaluating impact of data from radar networks on thunderstorm analysis and forecast. J. Atmos. Ocean Tech., 23, 46–66.

-----, S. Liu, and T. Yu, 2006b: Variational analysis of over-sampled dual-Doppler radial velocity data and application to the analysis of tornado circulations. J. Atmos. Ocean Tech., Under review.

Zrnic, D. S., 1975: Simulation of weatherlike Doppler spectra and signals. J. App. Meteor., 14, 619-620.

List of figures

been changed to allow both first and second trip echoes to be shown.

Figure 12. As in Figure 3, but for experiment EXP8, highlighting the storm structure observed at X-band.

Figure 13. PPI of returned power difference between CNTL and EXP8, showing clearly the range propagation effect of Rayleigh attenuation at X-band.

Figure 14. PPIs of (a) equivalent reflectivity factor, (b) spectrum width, (c) aliased Doppler velocity, and (d) non-aliased Doppler velocity for a radar located 3 km from the tornado using matched sampling. The black circle indicates the location and size of the tornado in the model.

Figure 15. As in Figure 14, but for the radar azimuthally oversampling by a factor of two.

Figure 16. As in Figure 14, but for a radar located 10 km from the tornado.

Figure 17. As in Figure 16, but for a radar azimuthally oversampling by a factor of two.

Figure 18. As in Figure 14, but for a radar located 30 km from the tornado.

Figure 19. As in Figure 18, but for a radar azimuthally oversampling by a factor of two.

Figure 20. As in Figure 14, but for a radar located 50 km from the tornado.

Figure 21. As in Figure 20, but for a radar azimuthally oversampling by a factor of two.

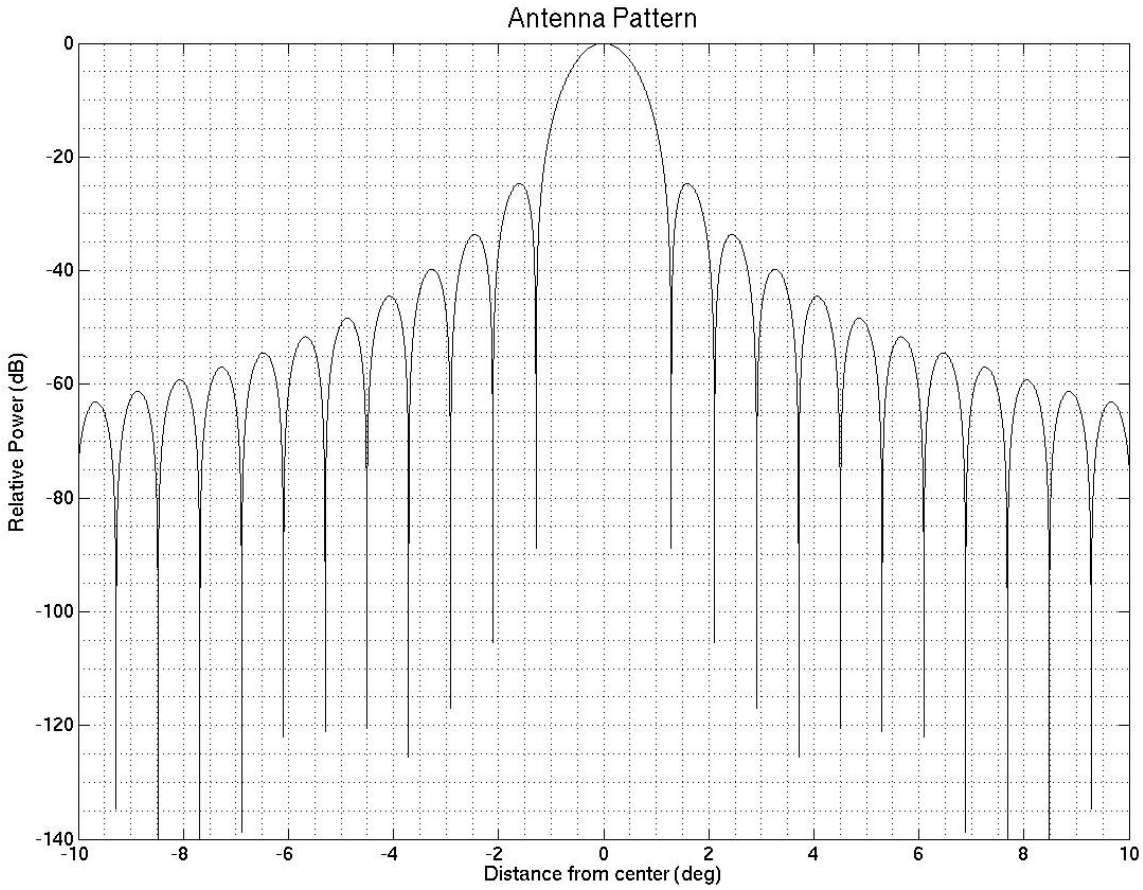

Figure 1. Emulator antenna pattern for a one-degree half-power beamwidth radar.

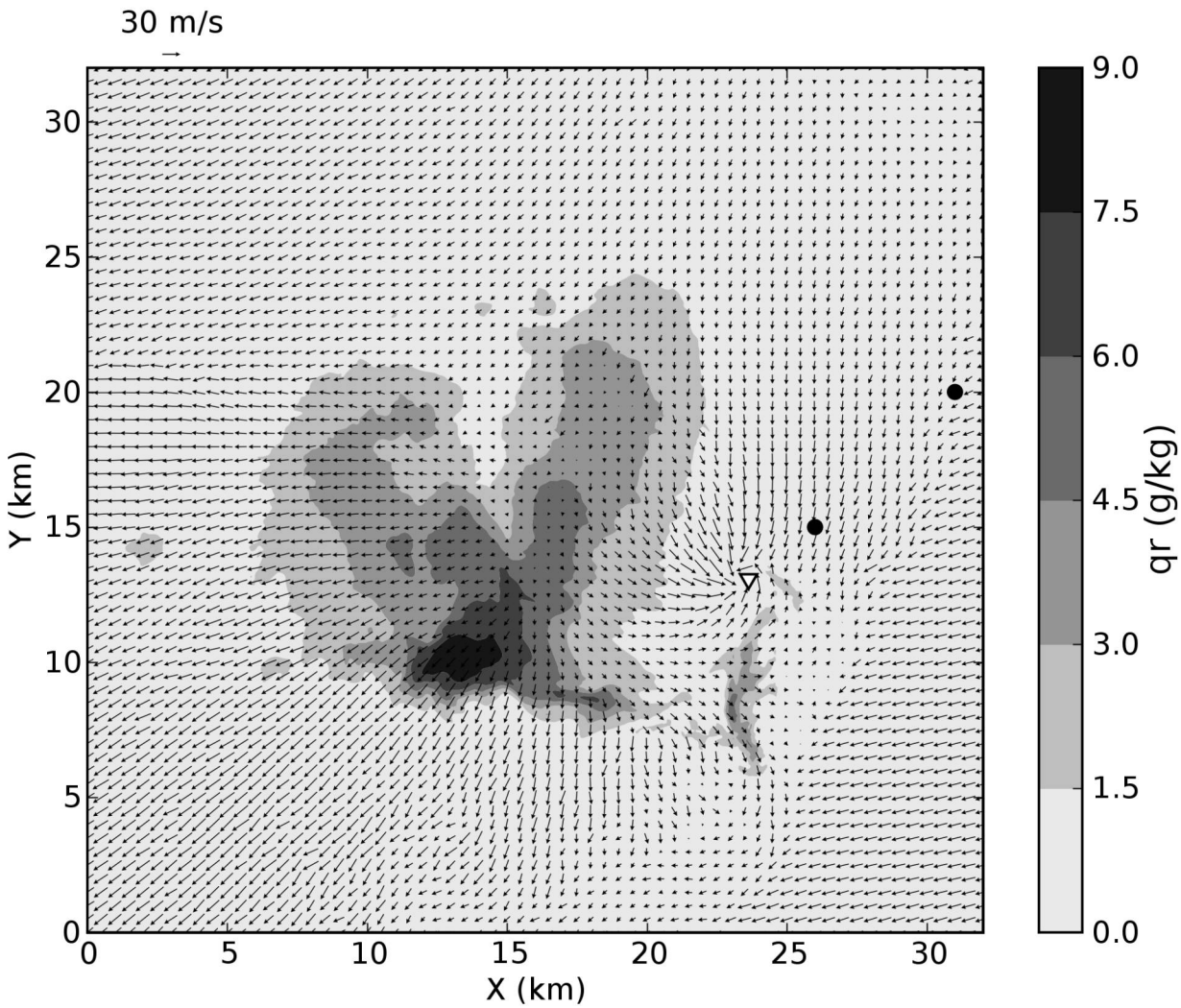

Figure 2. Model rain water mixing ratio (q_r) and vector velocity fields at 13500s into the simulation and 20 m height. The black dots represent radar locations at ranges of 3 km and 10 km. The inverted triangle represents the location of the tornado.

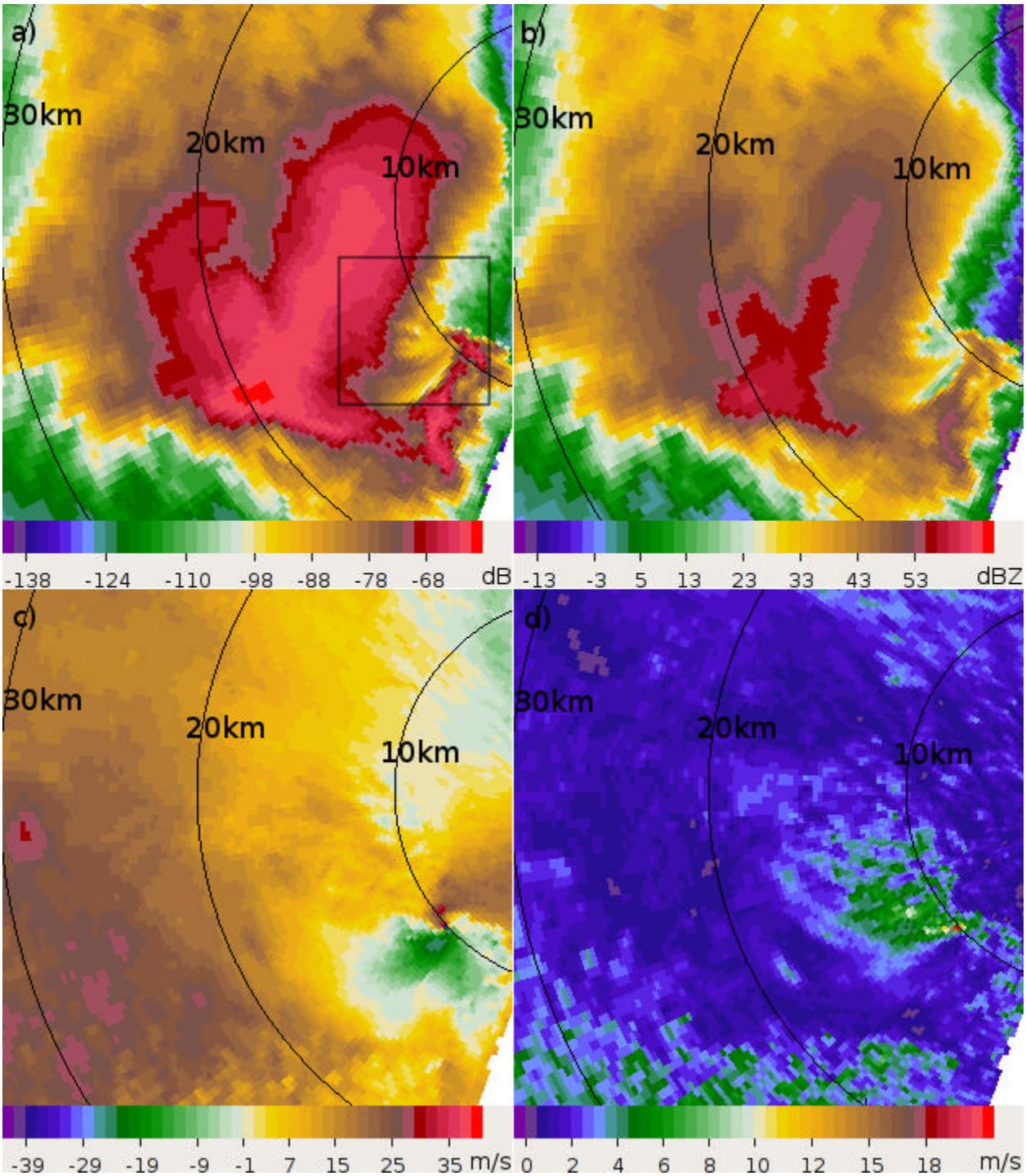

Figure 3. PPIs of (a) returned power (dB relative to 1 W), (b) equivalent reflectivity factor (Z_e), (c) Doppler velocity, and (d) spectrum width for control experiment CNTL. The box denotes the region shown in Figure 4, where the simulated tornado is found.

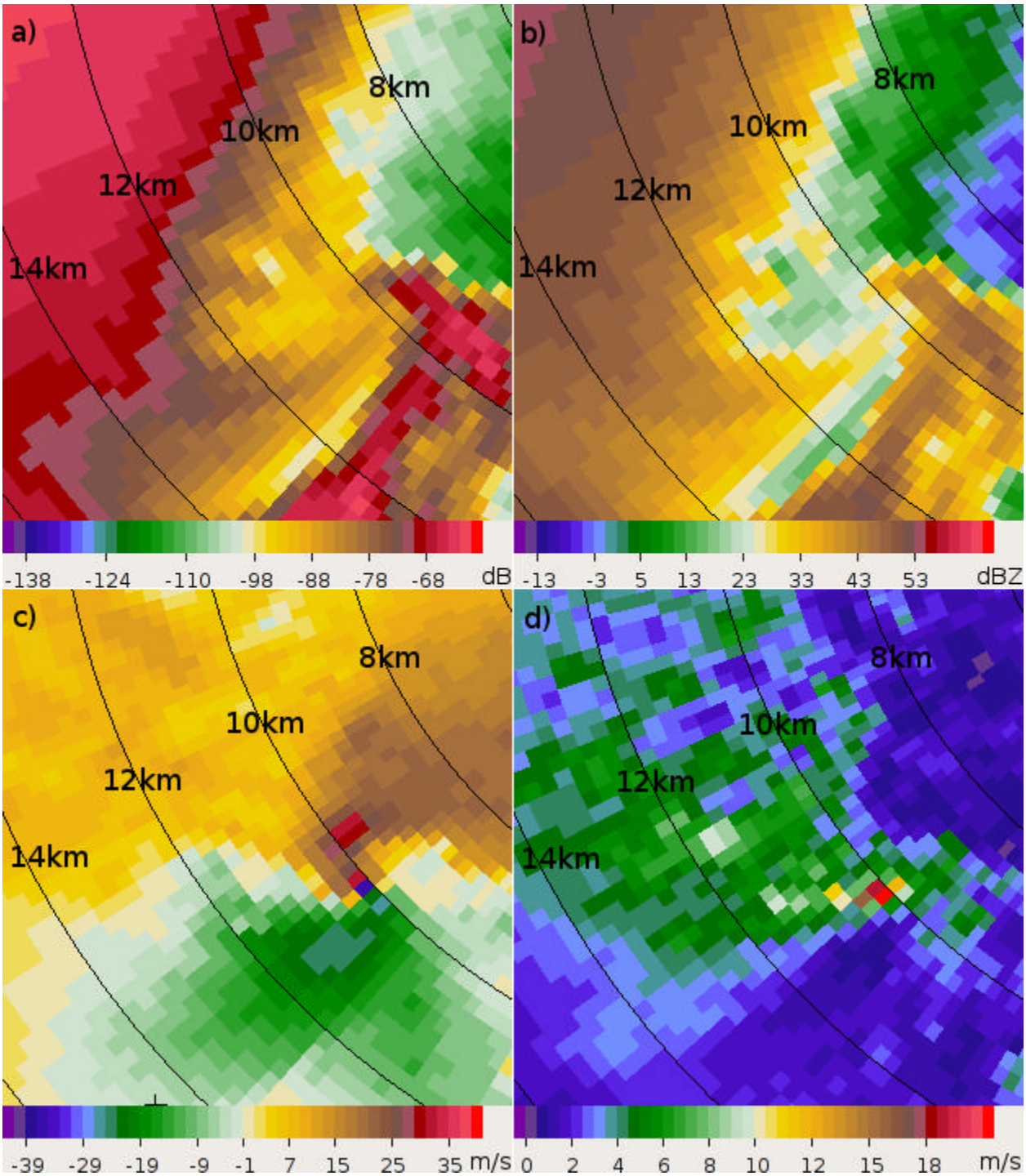

Figure 4. As in Figure 3, but magnified in to show more details in the region of mesocyclone and tornado.

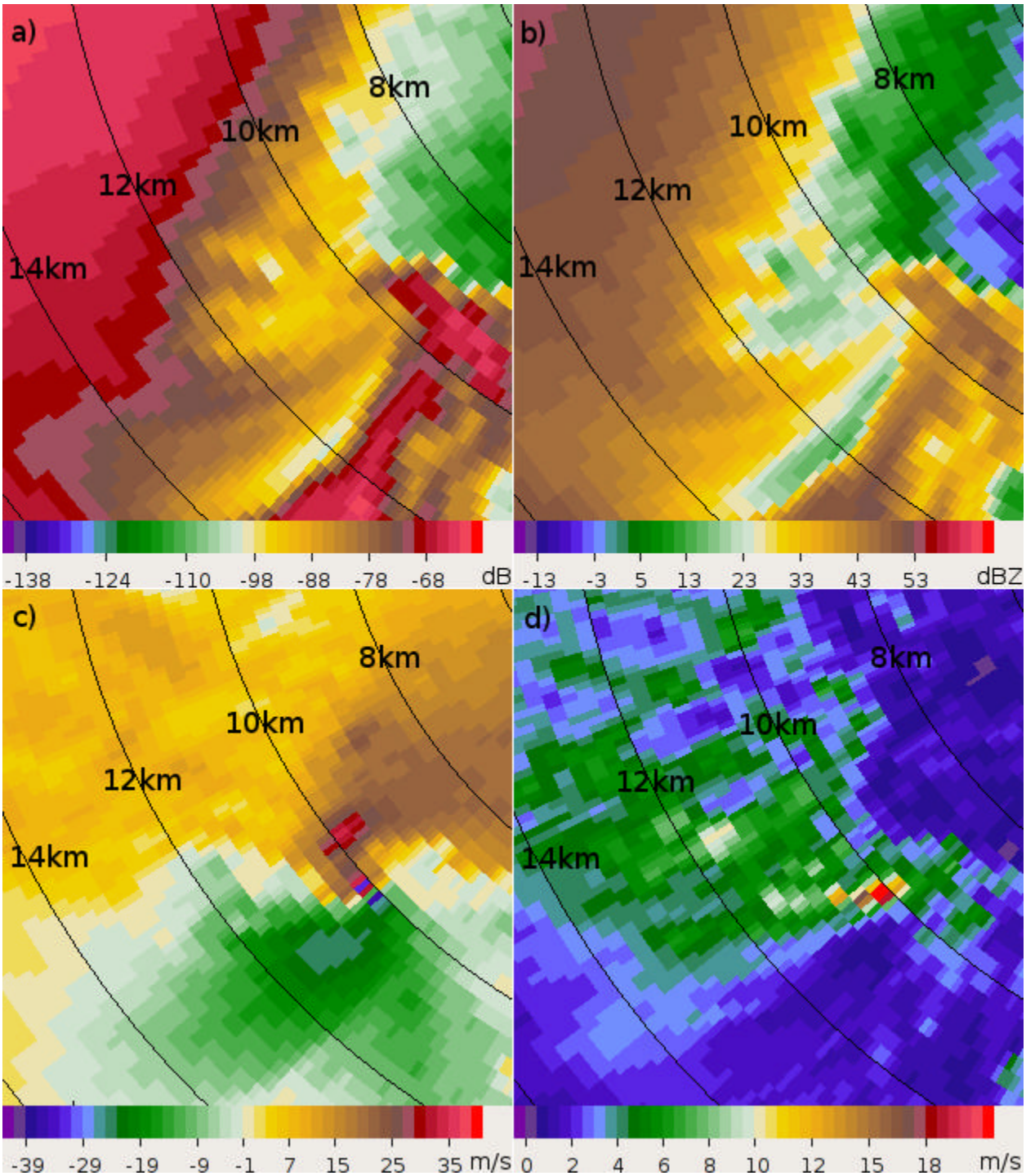

Figure 5. As in Figure 4, but for experiment EXP2, showing the effects of azimuthal oversampling.

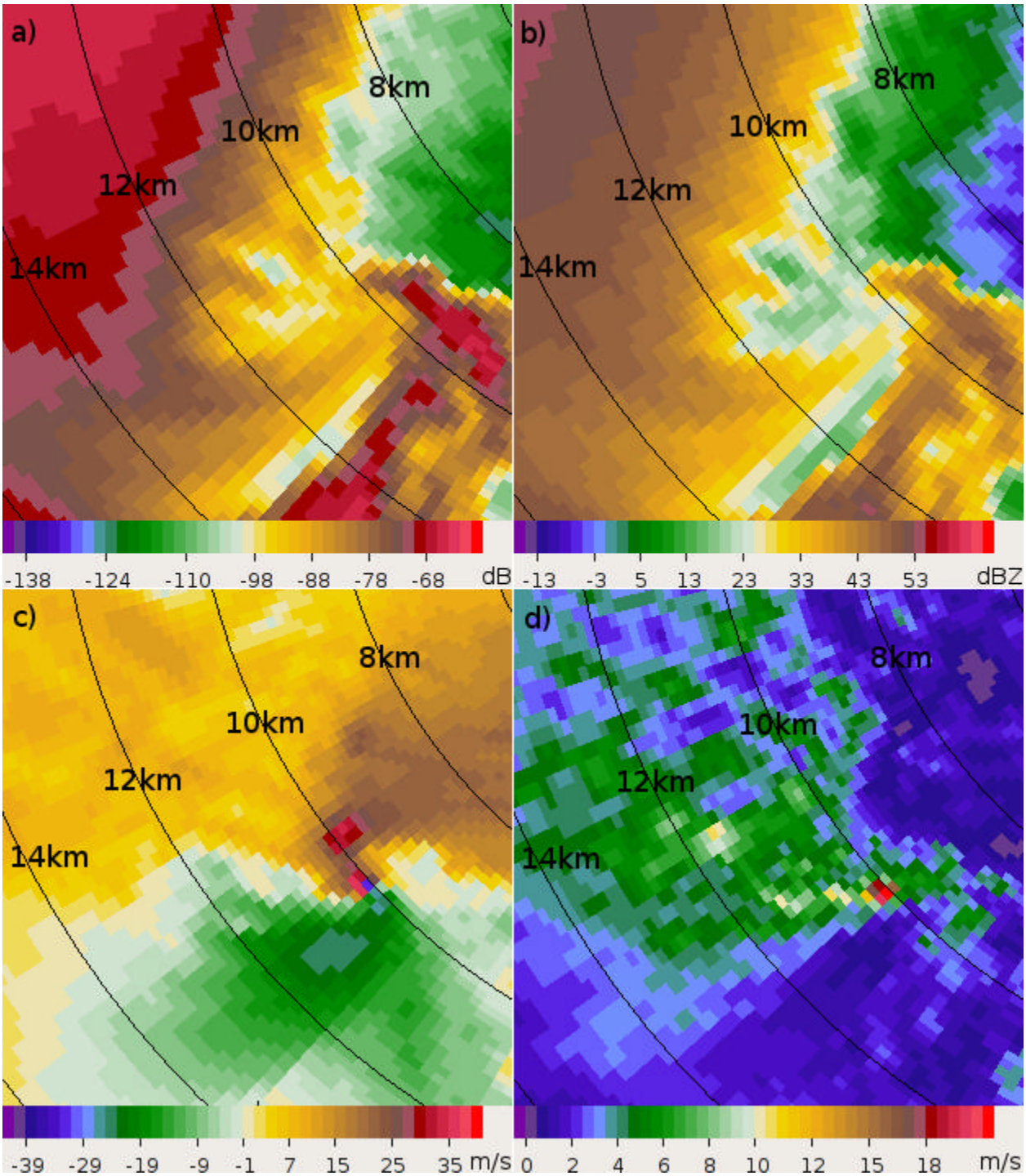

Figure 6. As in Figure 4, but for experiment EXP3, showing differences due to a shorter gate spacing and shorter pulse duration.

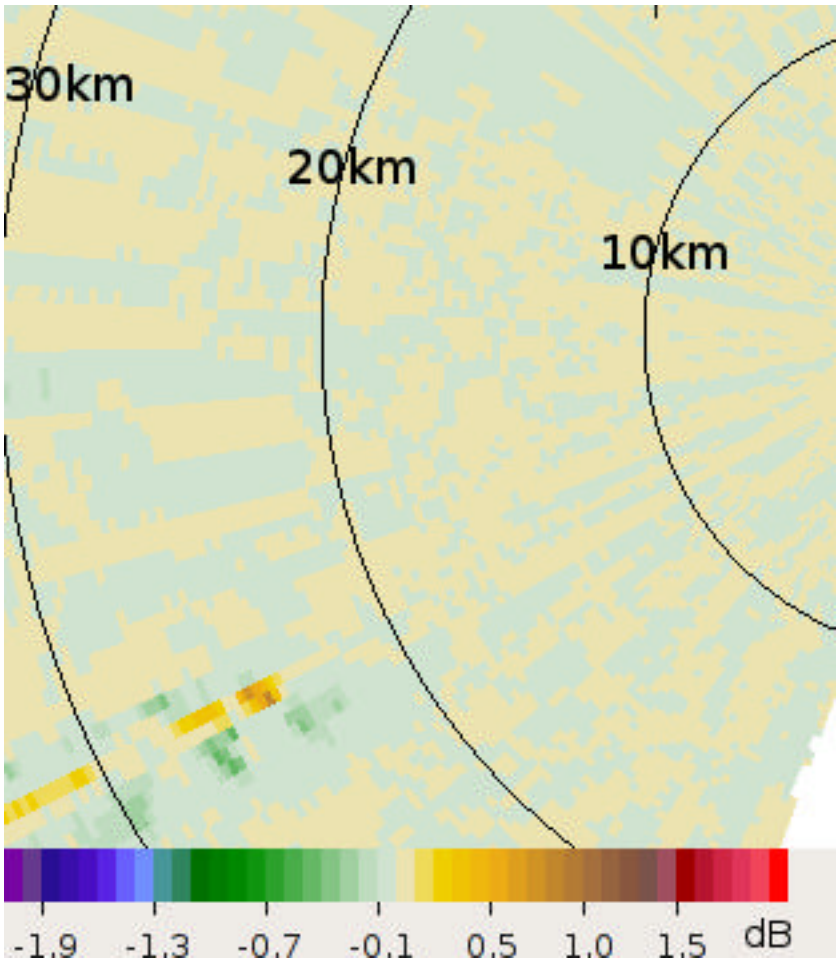

Figure 7. PPI of returned power difference between CNTL and EXP4 (CNTL subtracted from EXP4), showing overall minimal differences due to sidelobes. Areas where EXP4 has less returned power are due to numeric instability in the computations.

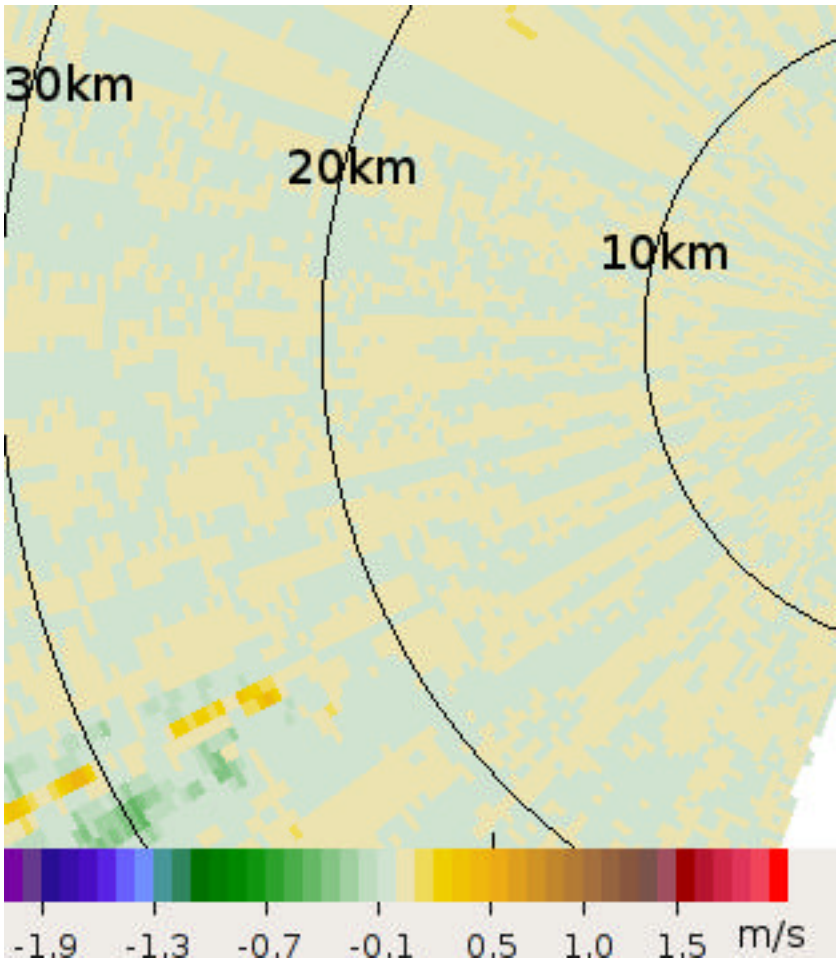

Figure 8. As in Figure 7 but for Doppler velocity difference, showing the small impact of sidelobes on measured Doppler velocity.

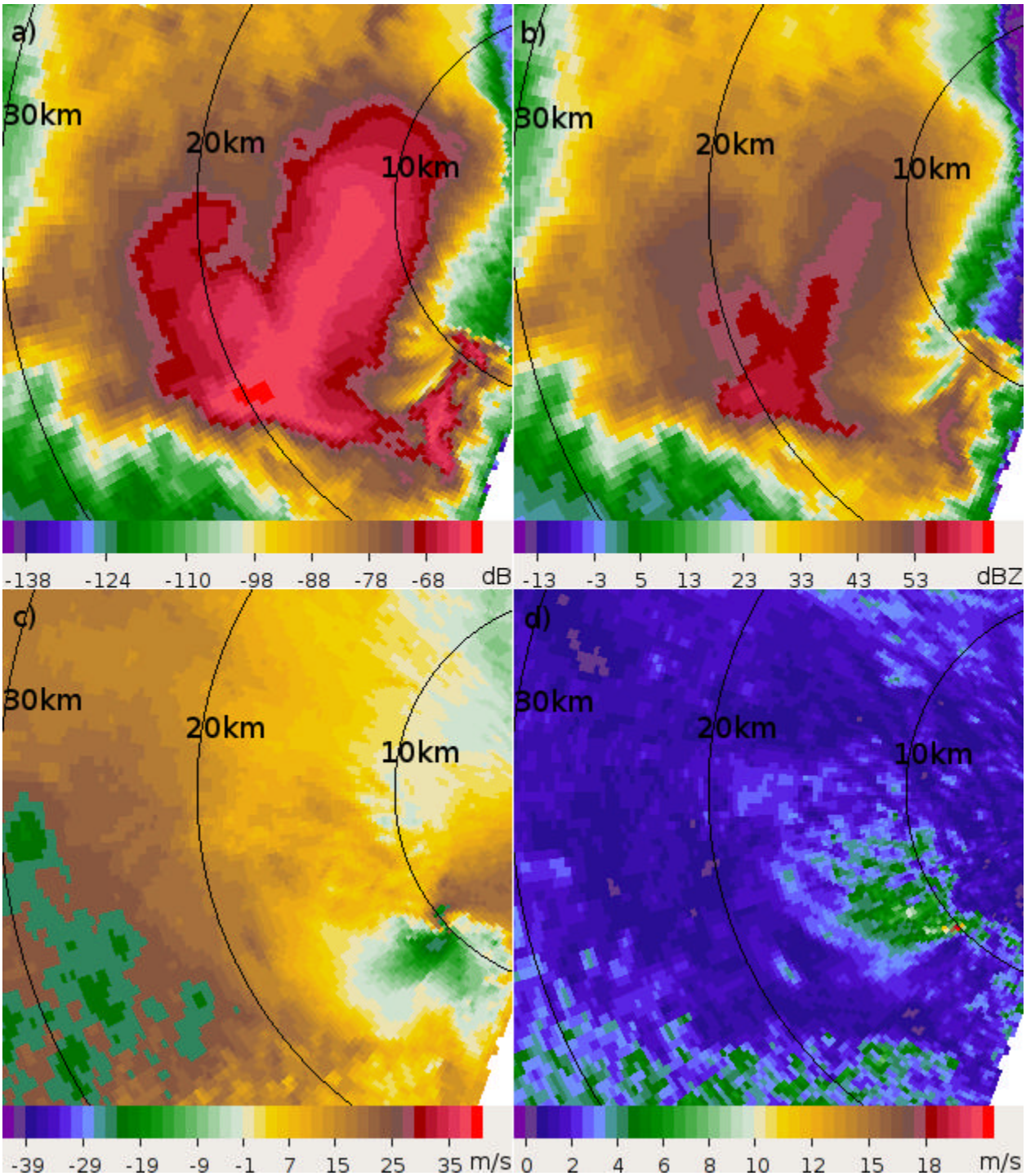

Figure 9. As in Figure 3, but for experiment EXP5, showing the impacts of reducing the PRF.

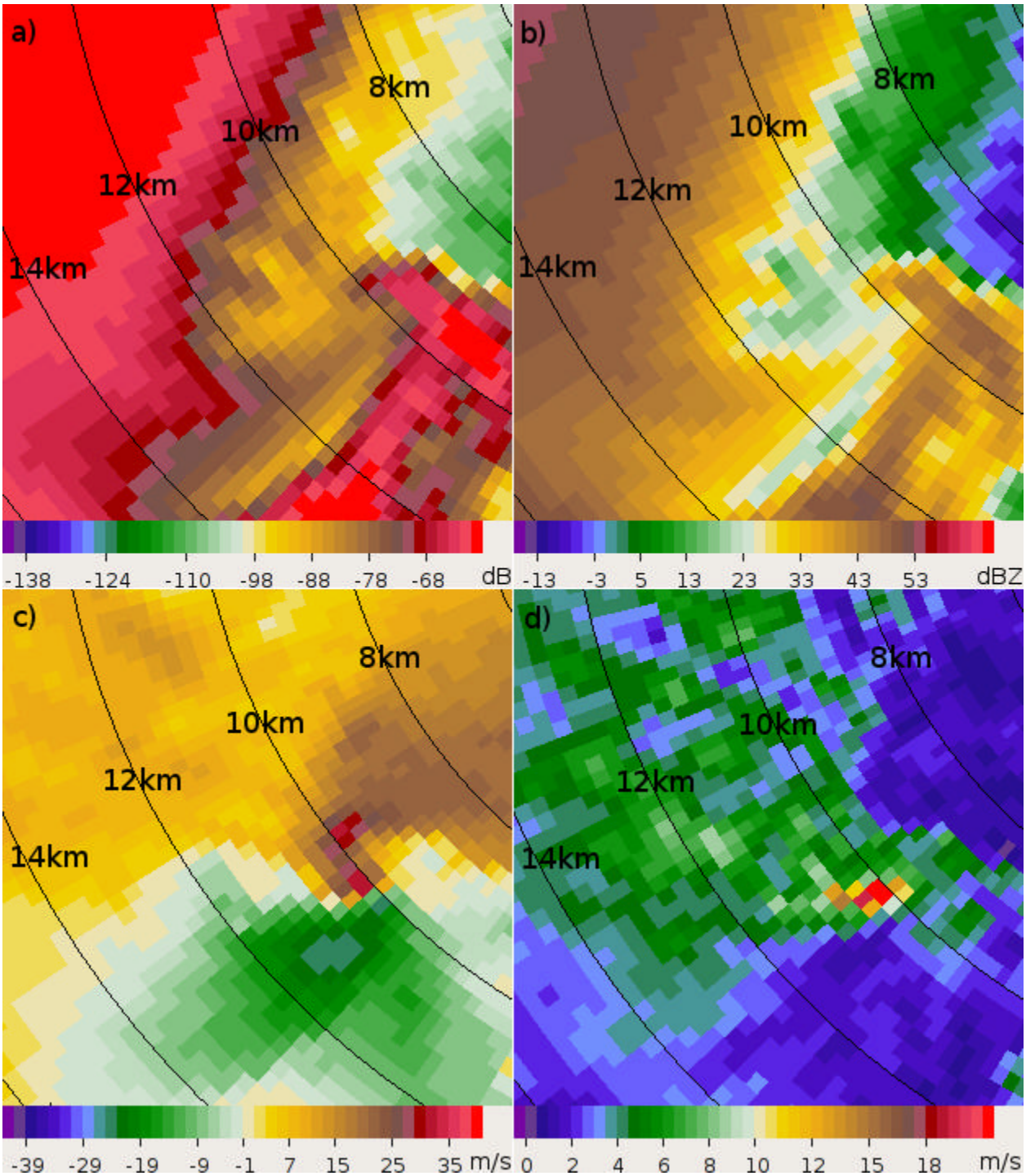

Figure 10. As in Figure 4, but for experiment EXP6, showing the impacts of changing the half-power beamwidth.

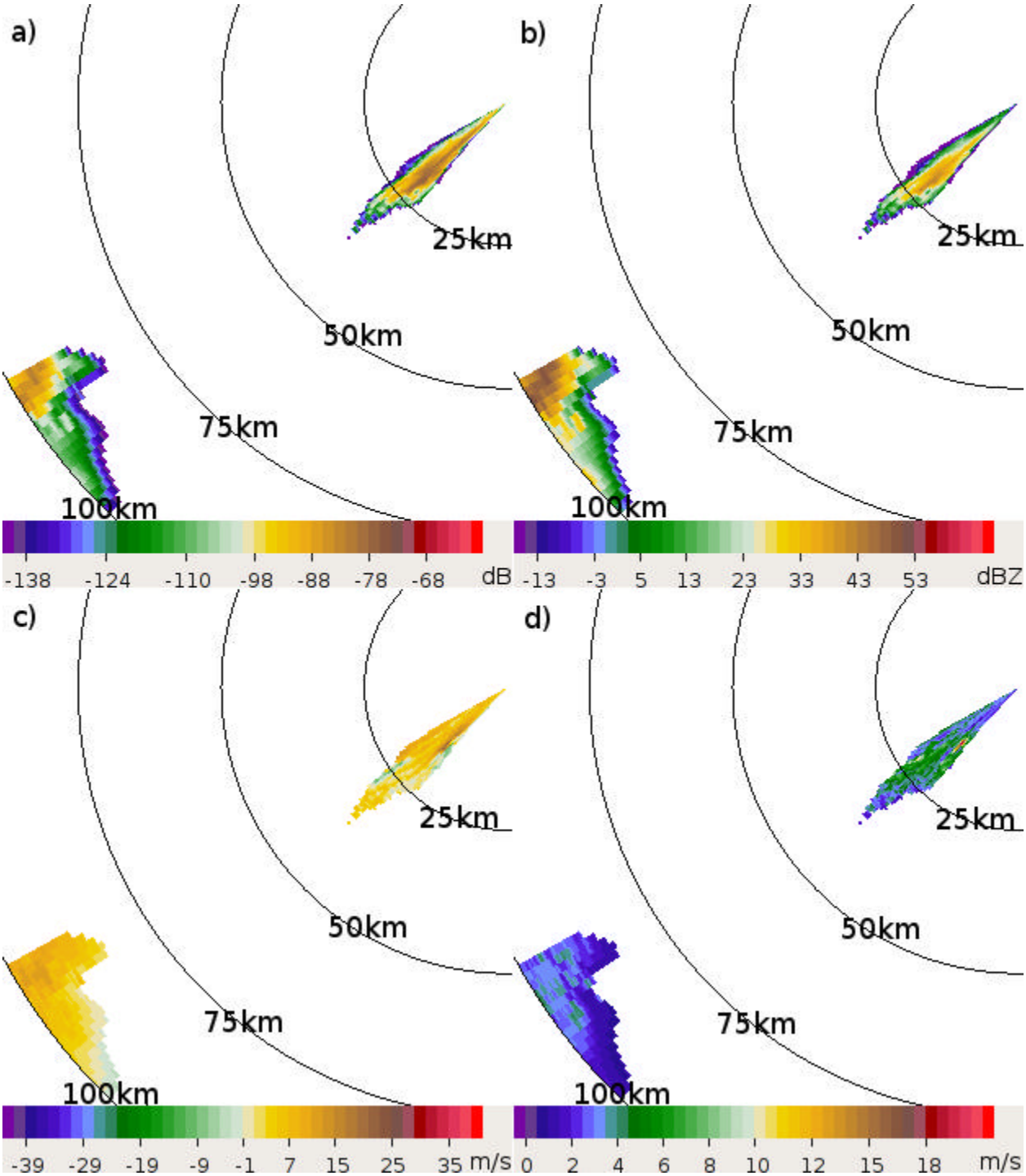

Figure 11. As in Figure 3, but for experiment EXP7, showing second trip echoes. The scale has been changed to allow both first and second trip echoes to be shown.

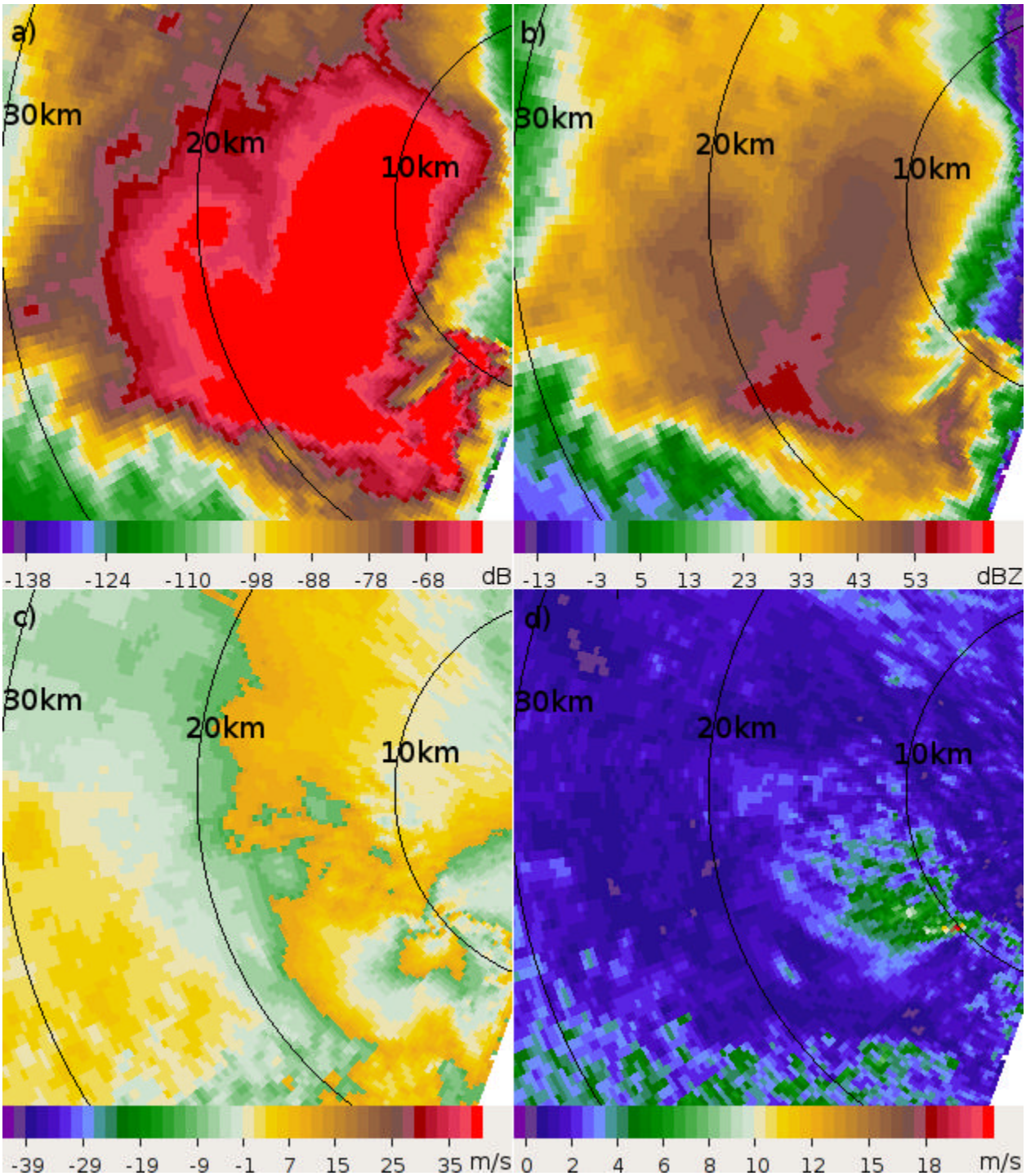

Figure 12. As in Figure 3, but for experiment EXP8, highlighting the storm structure observed at X-band.

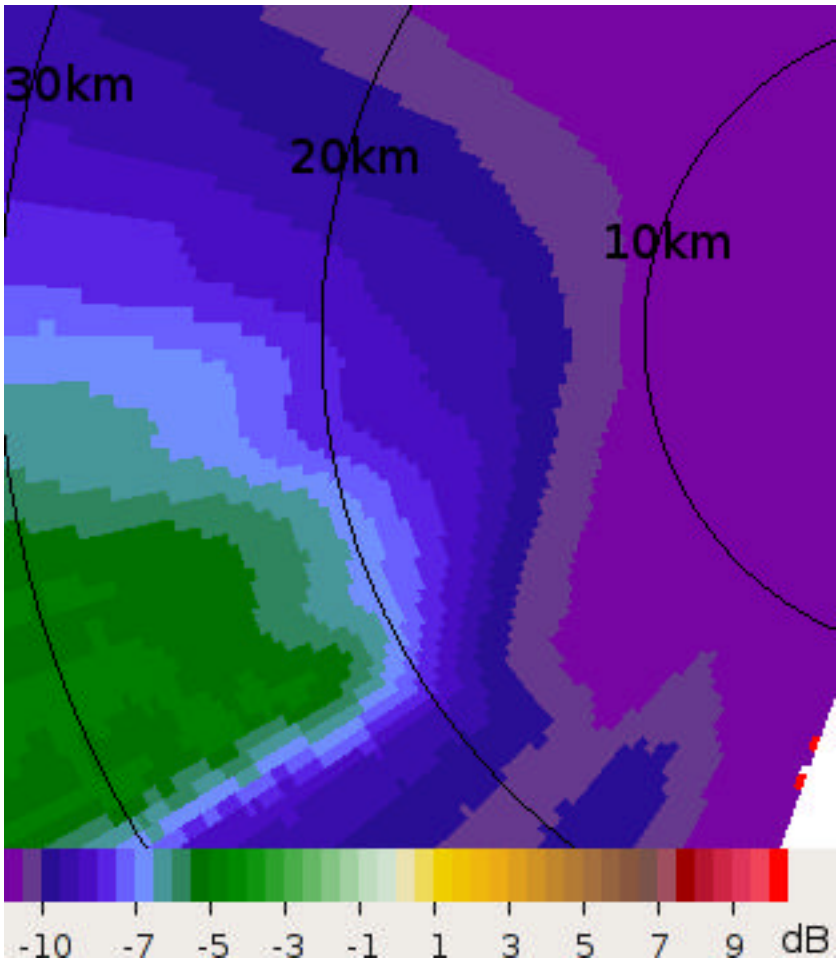

Figure 13. PPI of returned power difference between CNTL and EXP8, showing clearly the range propagation effect of Rayleigh attenuation at X-band.

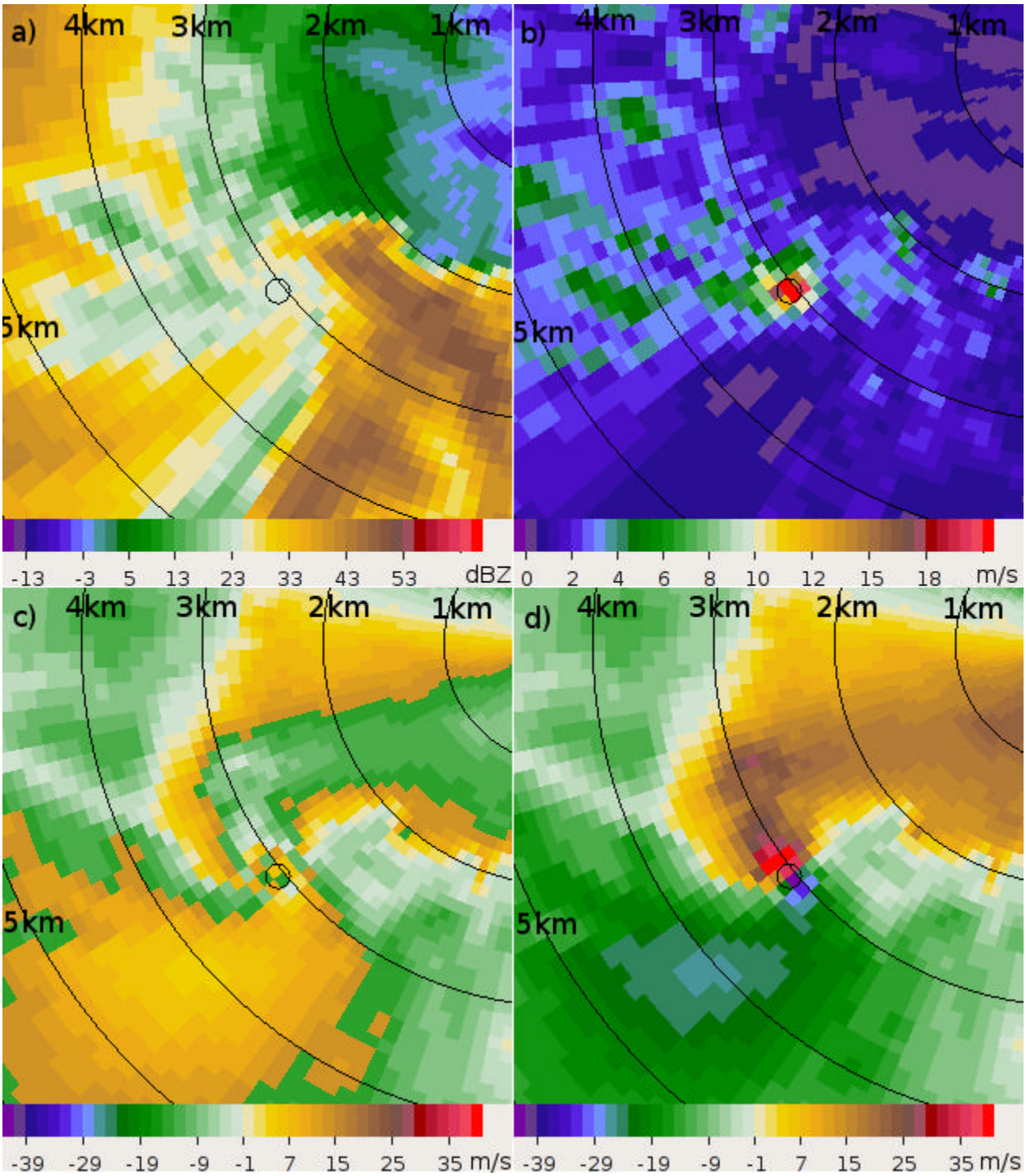

Figure 14. PPIs of (a) equivalent reflectivity factor, (b) spectrum width, (c) aliased Doppler velocity, and (d) non-aliased Doppler velocity for a radar located 3 km from the tornado using matched sampling. The black circle indicates the location and size of the tornado in the model.

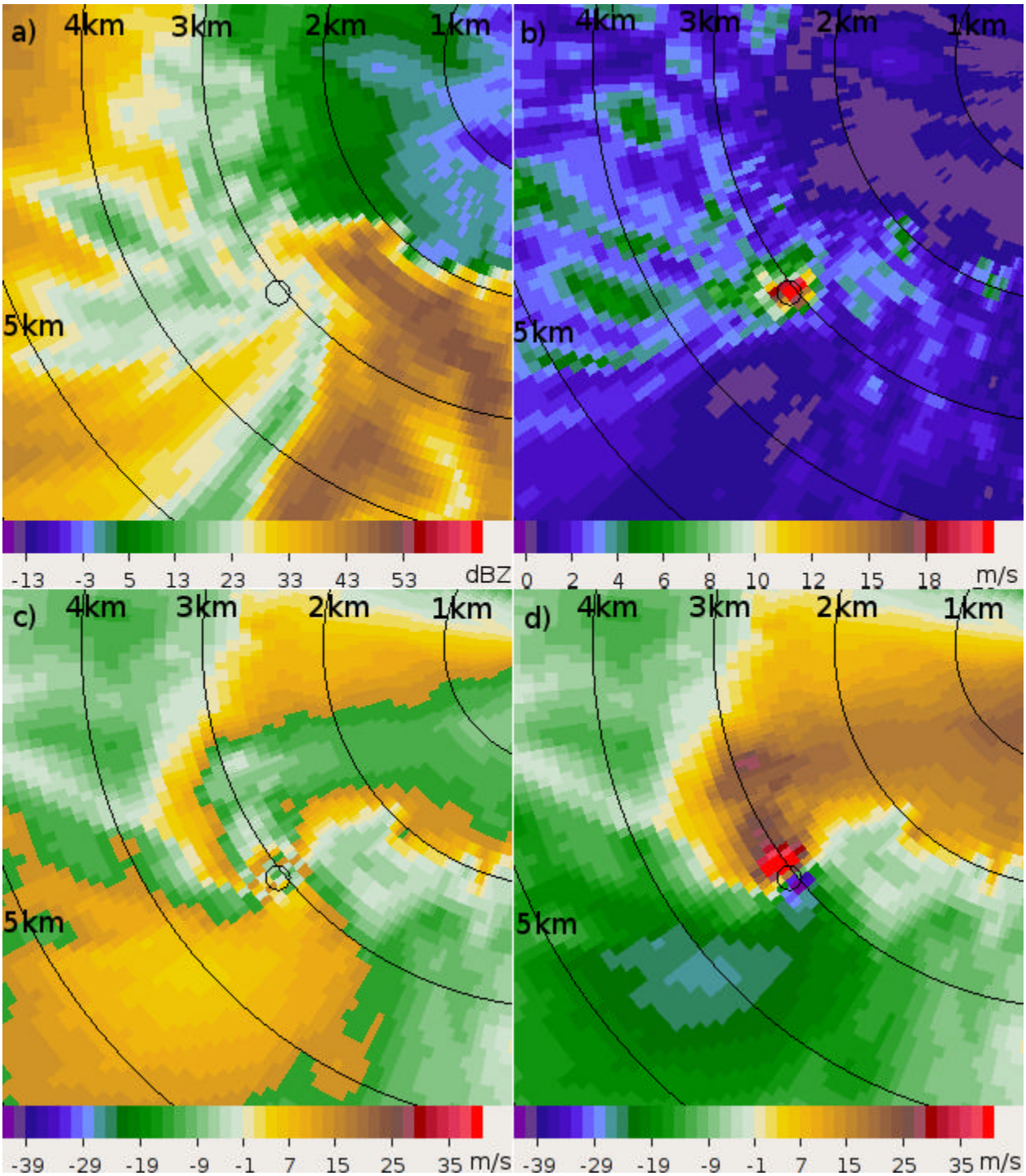

Figure 15. As in Figure 14, but for the radar azimuthally oversampling by a factor of two.

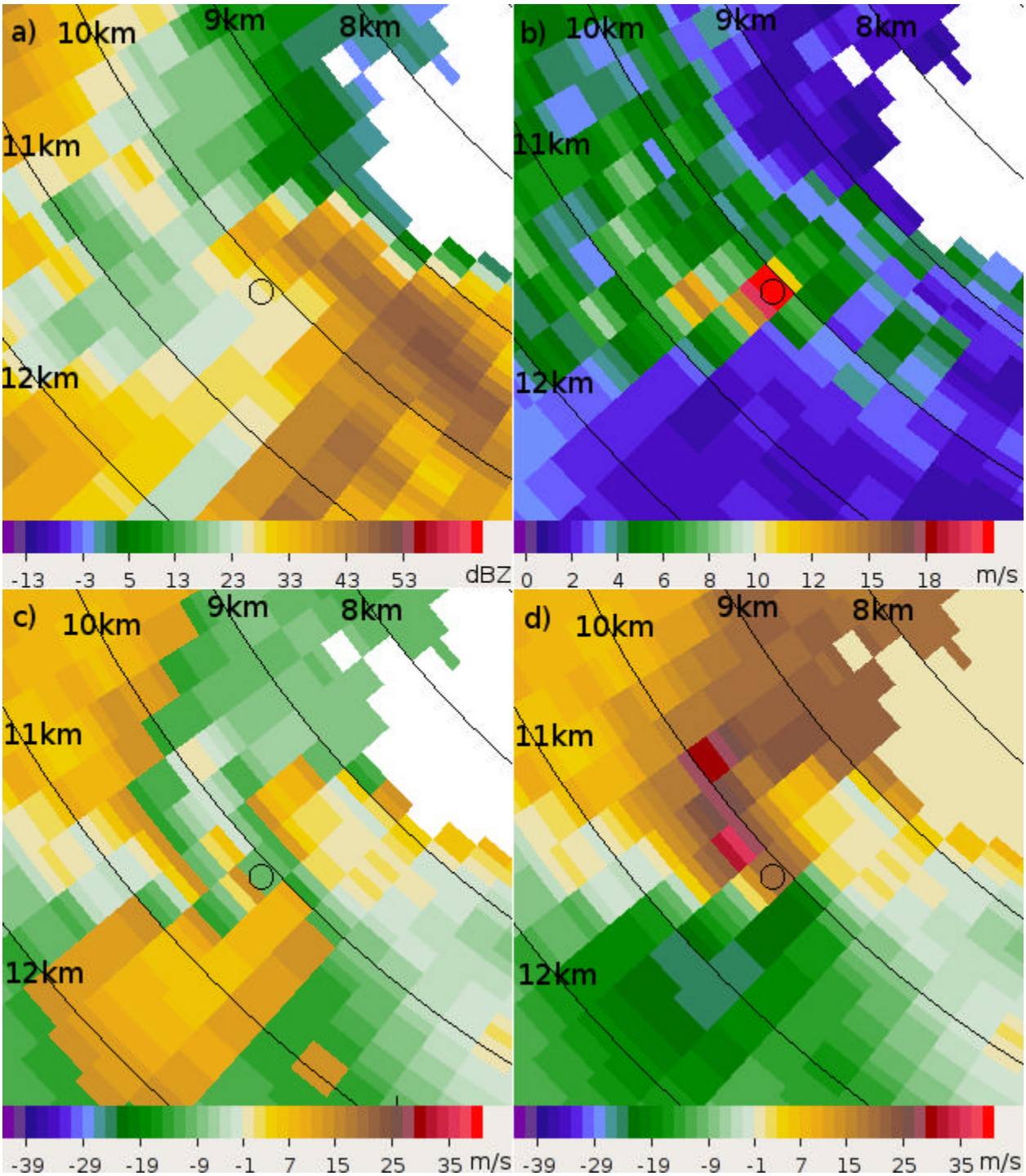

Figure 16. As in Figure 14, but for a radar located 10 km from the tornado.

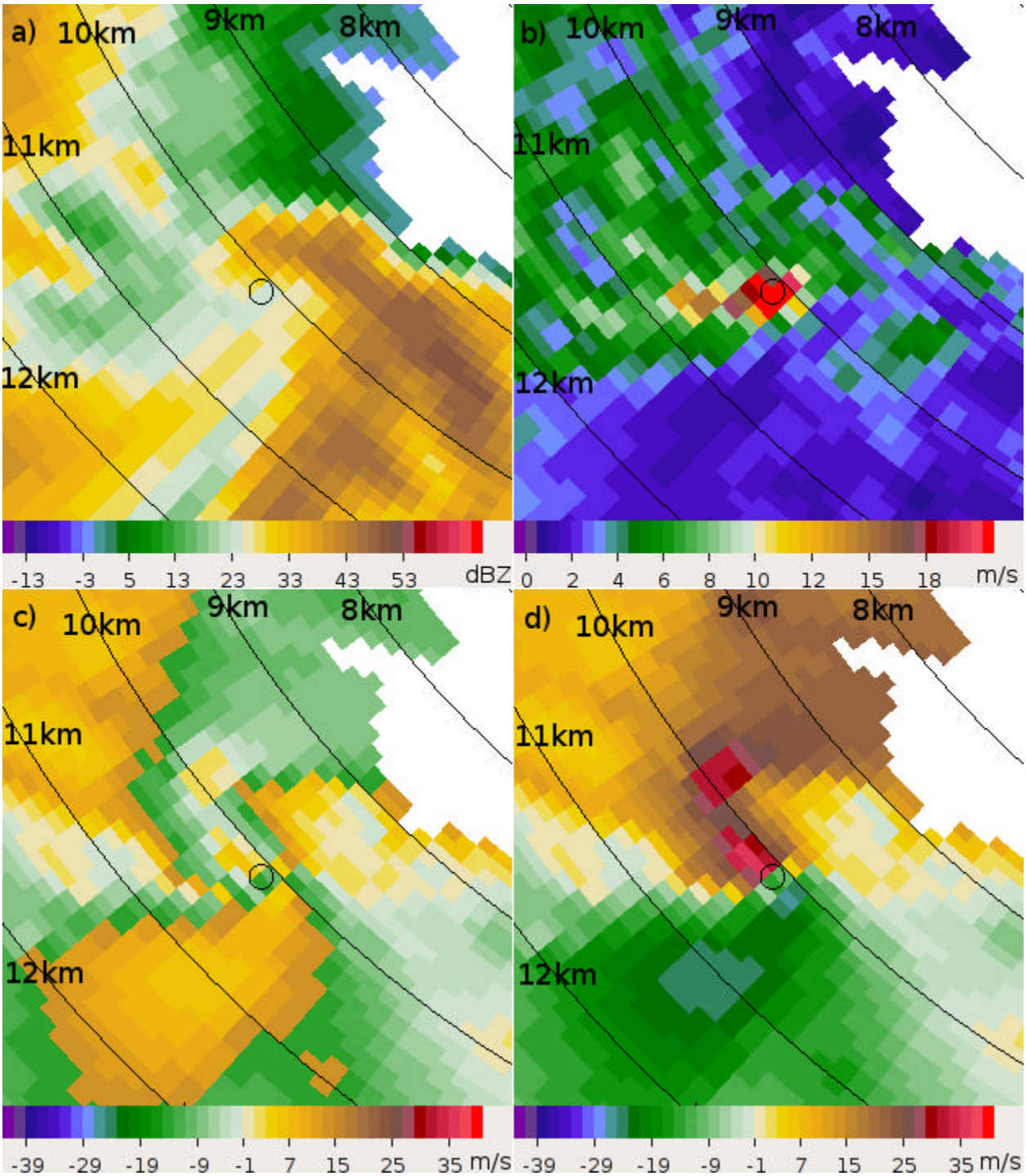

Figure 17. As in Figure 16, but for a radar azimuthally oversampling by a factor of two.

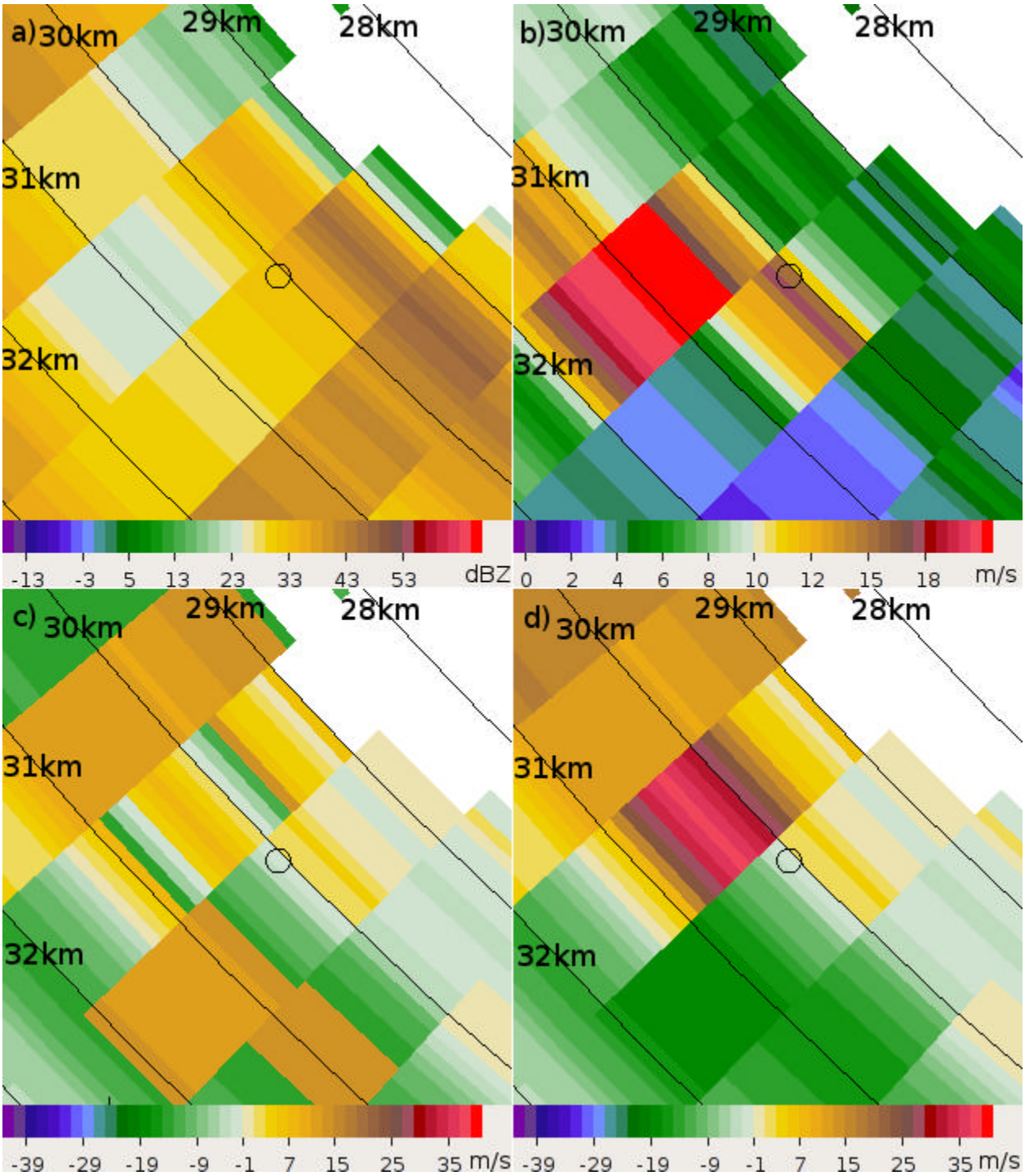

Figure 18. As in Figure 14, but for a radar located 30 km from the tornado.

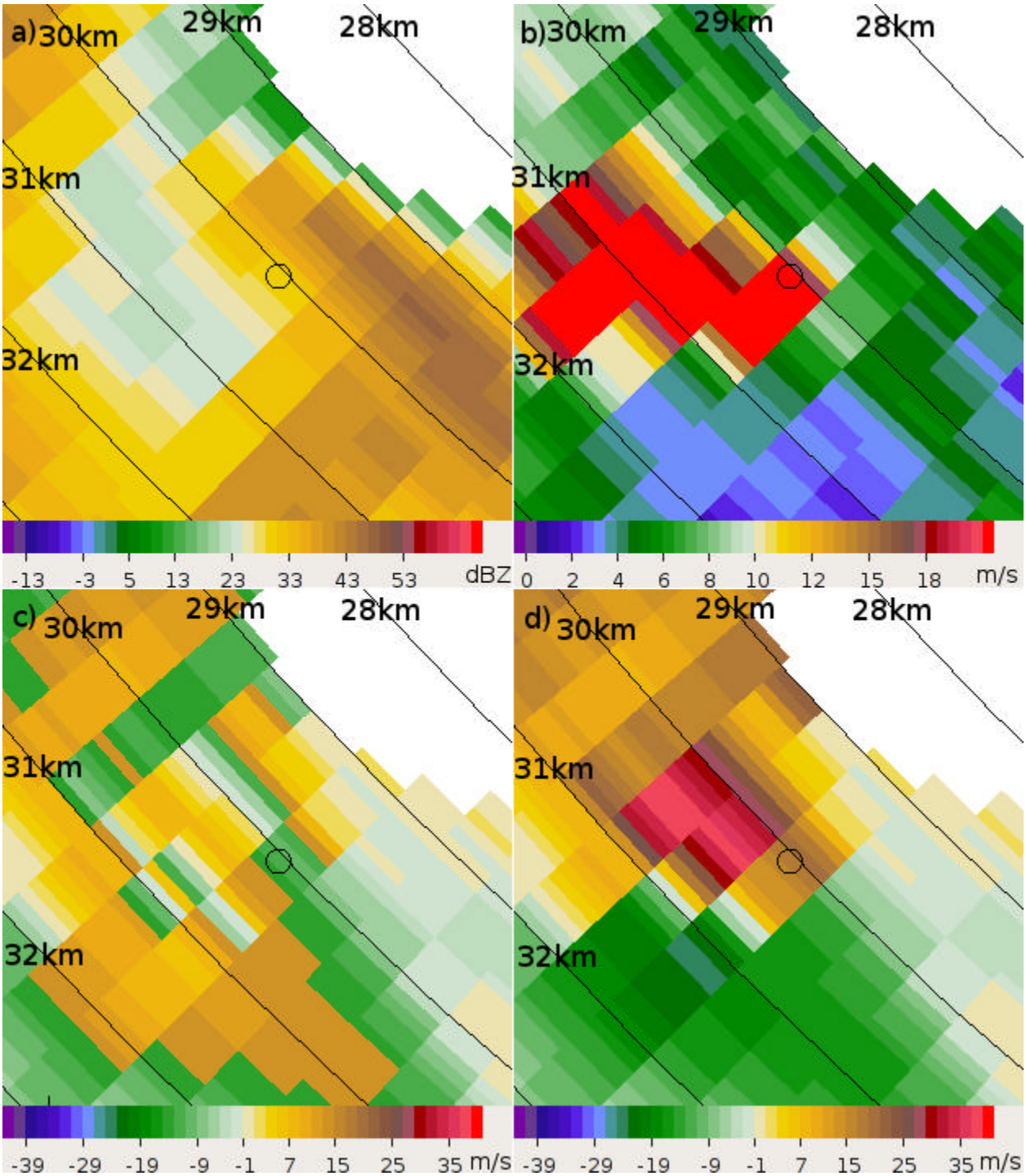

Figure 19. As in Figure 18, but for a radar azimuthally oversampling by a factor of two.

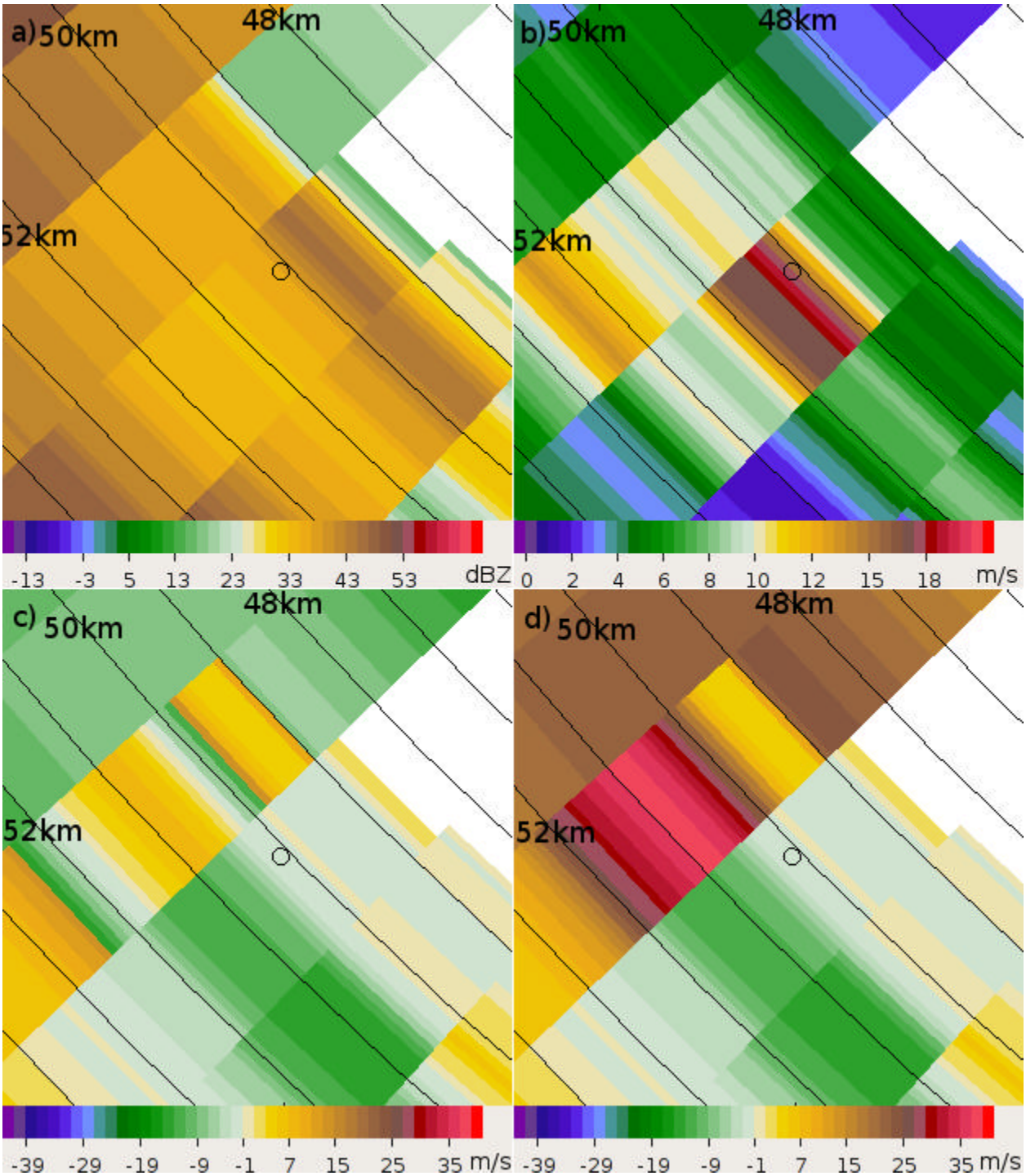

Figure 20. As in Figure 14, but for a radar located 50 km from the tornado.

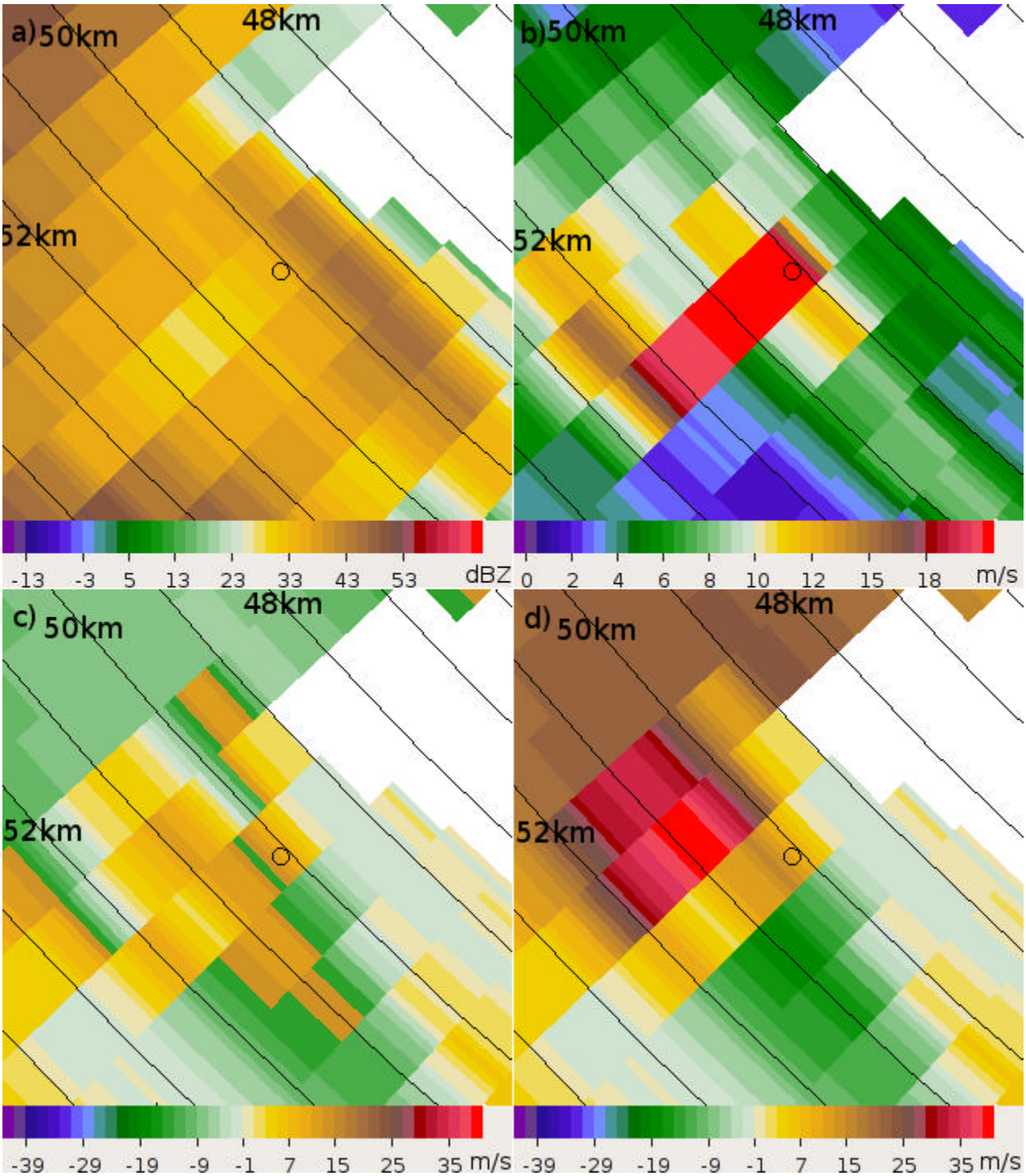

Figure 21. As in Figure 20, but for a radar azimuthally oversampling by a factor of two.

Table 1. Emulator control parameters.

Radar Parameters	**Scanning Strategy Parameters**
Location	Pulse repetition time (PRT)
Antenna beamwidth	Pulse length
Antenna gain (including sidelobes)	Antenna rotation rate
Wavelength	Number of pulses per radial
Transmit power	Radar gate spacing
Range to first gate	Scan fixed angle
Minimum detectable signal	Scan start and end angles

Table 2. Configuration parameters for each experiment.

Exp.	**λ (cm)**	**Beam-width (deg)**	**PRF (Hz)**	**Pulse Length (μs)**	**Rot. Rate (deg s^{-1})**	**Pulses Per Rad.**	**Gate Length (m)**	**ΔAz (deg)**	**V_{NYQ} (m s^{-1})**	**R_a (km)**
CNTL	10	1	1500	1.5	20	75	250	1.0	37.50	100
EXP2	10	1	1500	1.5	15	50	250	0.5	37.50	100
EXP 3	10	1	1500	.75	20	75	125	1.0	37.50	100
EXP 4	10	1	1500	1.5	20	75	250	1.0	37.50	100
EXP 5	10	1	1000	1.5	20	50	250	1.0	25.00	150
EXP 6	10	2	1500	1.5	20	75	250	1.0	37.50	100
EXP 7	10	1	1500	1.5	20	75	250	1.0	37.50	100
EXP 8	3	1	1500	1.5	20	75	250	1.0	11.25	100

Table 3. Configuration parameters for CASA radars.

Radar Parameter	**Matched Sampling**	**Oversampled**
λ (cm)	3	3
Beamwidth (deg)	2	2
PRF (Hz)	2000	2000
Rot. Rate (deg s^{-1})	40	40
Pulses Per Rad.	100	50
Pulse Length (μs)	.5	.5
Gate Length (m)	100	100
ΔAz (deg)	2	1

Table 4. Calculated tornado parameters for emulated CASA radars.

Experiment (radar range and oversampling)	**V_{max} (m s^{-1})**	**ΔV (m s^{-1})**	**D (m)**	**2 $\Delta V/D$ (s^{-1})**
3km, Matched	49.1	93.3	216	0.864
3km, Oversampled	55.7	110.6	216	1.024
10km, Matched	35.2	57.6	705	0.163
10km, Oversampled	36.3	62.7	529	0.237
30km, Matched	31.8	33.4	1047	0.064
30km, Oversampled	32.3	42.7	1047	0.082
50km, Matched	27.5	29.5	1749	0.034
50km, Oversampled	28.5	38.6	1749	0.044